Planetary boundary layer height modulates aerosol - water interactions during winter in the megacity of Delhi

Subha S Raj[1,1], Ovid Krüger[2,2], Amit Sharma[3,3], Upasana Panda[4,4], Christopher Pöhlker[2,2], David Walter[5,5], Jan-David Förster[2,2], Rishi Pal Singh[6,6], Swetha S[7,7], Thomas Klimach[2,2], Eoghan Darbyshire[8,8], Scot T. Martin[9,9], Gordon McFiggans[10,10], Hugh Coe[10,10], James D Allan[10,10], Ravikrishna R[1,1], Vijay Kumar Soni[11,11], Hang Su[2,2], Meinrat O. Andreae[2,2], Ulrich Pöschl[2,2], Mira L. Pöhlker[2,2], and Sachin S. Gunthe[12,12]

[1]Indian Institute of Technology Madras
[2]Max Planck Institute for Chemistry
[3]Indian Institute of Technology Jodhpur
[4]CSIR Institute of Minerals and Materials Technology
[5]Max-Planck-Institut für Chemie
[6]India Meteorological Department New Delhi
[7]CSIR Fourth Paradigm Institute
[8]The Conflict and Environment Observatory
[9]Harvard University
[10]University of Manchester
[11]India Meteorological Department
[12]Environmental and Water Resources Engineering Division, Department of Civil Engineering, Indian Institute of Technology Madras, Chennai 600036, India.

November 30, 2022

Abstract

The Indo-Gangetic Plain (IGP) is one of the dominant sources of air pollution worldwide. During winter, the variations in planetary boundary layer (PBL) height, driven by a strong radiative thermal inversion, affect the regional air pollution dispersion. To date, measurements of aerosol-water vapour interactions, especially cloud condensation nuclei (CCN) activity, are limited in the Indian sub-continent, causing large uncertainties in the radiative forcing estimates of aerosol-cloud interactions. We present the results of a one-month field campaign (February-March 2018) in the megacity, Delhi, a significant polluter in the IGP. We measured the composition of fine particulate matter (PM1) and size-resolved CCN properties over a wide range of water vapour supersaturations. The analysis includes PBL modelling, backward trajectories, and fire spots to elucidate the influence of PBL and air mass origins on the aerosols. The aerosol properties depended strongly on the PBL height, and a simple power-law fit could parameterize the observed correlations of PM1 mass, aerosol particle number, and CCN number with PBL height, indicating PBL induced changes in aerosol accumulation. The low inorganic mass fractions, low aerosol hygroscopicity and high externally mixed weakly CCN-active particles under low PBL height (<100 m) indicated the influence of the PBL on aerosol aging processes. In contrast, aerosol properties did not depend strongly on air mass origins or wind direction, implying that the observed aerosol and CCN are from local emissions. An error function could parameterize the relationship between CCN number and supersaturation throughout the campaign.

Planetary boundary layer height modulates aerosol – water vapour interactions during winter in the megacity of Delhi

Subha S. Raj[1,2], Ovid O. Krüger[3], Amit Sharma[1,a], Upasana Panda[1,4], Christopher Pöhlker[3], David Walter[3], Jan-David Förster[3], Rishi Pal Singh[5], Swetha S.[1,b], Thomas Klimach[3], Eoghan Darbyshire[6,c], Scot T. Martin[7,8], Gordon McFiggans[6], Hugh Coe[6], James Allan[6,9], Ravikrishna R.[10,2], Vijay Kumar Soni[5], Hang Su[3], Meinrat O. Andreae[3,11,12], Ulrich Pöschl[3], Mira L. Pöhlker[3]and Sachin S. Gunthe[1,2]

[1]EWRE Division, Department of Civil Engineering, Indian Institute of Technology Madras, Chennai, India
[2]Laboratory for Atmospheric and Climate Sciences, Indian Institute of Technology Madras, Chennai, India
[3]Multiphase Chemistry and Biogeochemistry Departments, Max Planck Institute for Chemistry, Mainz, Germany
[4]Department of Environment and Sustainability, CSIR Institute of Minerals and Materials Technology, Bhubaneswar, India
[5]India Meteorological Department, New Delhi, India
[6]Department of Earth and Environmental Sciences, School of Natural Sciences, University of Manchester, Manchester, UK
[7]John A. Paulson School of Engineering and Applied Sciences, Harvard University, Cambridge, MA, USA
[8]Department of Earth and Planetary Sciences, Harvard University, Cambridge, MA, USA
[9]National Centre for Atmospheric Science, University of Manchester, Manchester, UK
[10]Department of Chemical Engineering, Indian Institute of Technology Madras, Chennai, India
[11]Scripps Institution of Oceanography, University of California San Diego, La Jolla, CA, USA
[12]Department of Geology and Geophysics, King Saud University, Riyadh, Saudi Arabia
[a]now at: Department of Civil and Infrastructure Engineering, Indian Institute of Technology Jodhpur, Karwar, Jodhpur, India
[b]now at: CSIR Fourth Paradigm Institute, Bengaluru, India
[c]now at: The Conflict and Environment Observatory, Hebden Bridge, West Yorkshire, UK

Key Points:

- Parameterizing CCN activity, and the relation between planetary boundary layer height (H_{BL}) and CCN loading in Delhi.
- H_{BL} is the major driving force of aerosol accumulation and aging processes in Delhi during late winter.
- The prominent accumulation mode in the aerosol size distribution compensates for lower aerosol hygroscopicity under low H_{BL} and therefore maintains high CCN efficiency during late winter in Delhi.

Corresponding author: Subha S. Raj, subhasraj89@gmail.com

Corresponding author: Mira L. Pöhlker, m.pohlker@mpic.de

Corresponding author: Sachin S. Gunthe, s.gunthe@iitm.ac.in

Abstract

The Indo-Gangetic Plain (IGP) is one of the dominant sources of air pollution worldwide. During winter, the variations in planetary boundary layer (PBL) height, driven by a strong radiative thermal inversion, affect the regional air pollution dispersion. To date, measurements of aerosol–water vapour interactions, especially cloud condensation nuclei (CCN) activity, are limited in the Indian sub-continent, causing large uncertainties in the radiative forcing estimates of aerosol-cloud interactions. We present the results of a one-month field campaign (February-March 2018) in the megacity, Delhi, a significant polluter in the IGP. We measured the composition of fine particulate matter (PM1) and size-resolved CCN properties over a wide range of water vapour supersaturations. The analysis includes PBL modelling, backward trajectories, and fire spots to elucidate the influence of PBL and air mass origins on the aerosols. The aerosol properties depended strongly on the PBL height, and a simple power-law fit could parameterize the observed correlations of PM1 mass, aerosol particle number, and CCN number with PBL height, indicating PBL induced changes in aerosol accumulation. The low inorganic mass fractions, low aerosol hygroscopicity and high externally mixed weakly CCN-active particles under low PBL height (<100 m) indicated the influence of the PBL on aerosol aging processes. In contrast, aerosol properties did not depend strongly on air mass origins or wind direction, implying that the observed aerosol and CCN are from local emissions. An error function could parameterize the relationship between CCN number and supersaturation throughout the campaign.

1 Introduction

The megacity of Delhi is located within the Indo-Gangetic Plain (IGP) and is one of the major sources of anthropogenic air pollution. It is a continental metropolitan area in a large valley south of the Himalayas, which causes the air masses to be constrained within the IGP (Figure 1). The air masses are vulnerable to high levels of particulate matter emissions from the megacity all year round (Bhandari et al., 2020), since it is a fast-growing urban agglomeration (Jain et al., 2016; Paul et al., 2021). During winter, a strong radiative thermal inversion causes the megacity to be enveloped by a shallow planetary boundary layer (PBL) in the nighttime, resulting in high relative humidity (RH) and aerosol mass burden (Arun et al., 2018; Murthy et al., 2020). The cold, humid and polluted conditions coupled with low wind speeds make the landlocked atmosphere conducive to fog and haze formation (Dhangar et al., 2021; Ojha et al., 2020; Dumka et al., 2019). Moreover, the aerosols in Delhi have enhanced water uptake ability as reported in the companion study by Gunthe et al. (2021), which can facilitate multiphase processes for formation of aerosols and thereby cause drastic visibility deterioration. Aerosol–PBL interactions in other megacities have also been associated with poor air quality caused by fog and haze during winter (Cheng et al., 2016; H. Su et al., 2020; T. Su et al., 2020; Tie et al., 2017; Zheng et al., 2015). In general, urban areas have enhanced concentration of fine aerosol particles, which are detrimental to public health (Lelieveld et al., 2020), and extensive anthropogenic gaseous emissions, which can further affect cloud activation responses of aerosols (Pöschl, 2005).

The spatial heterogeneity of cloud condensation nuclei (CCN) activity is not suitably captured in the sub-grids of climate models, which results in uncertainties associated with the estimates of their atmospheric responses to climate change (Boucher et al., 2013). This uncertainty is expected to be large in the Indian sub-continent due to the variety of topographical features like high mountains, low-lying coastal plains, the peninsular plateau, and human settlements ranging from rural towns and villages to metropolitan cities. Nevertheless, realistic formulations of CCN activity from direct measurements of CCN properties in size-resolved mode have not yet been reported over this part of the globe for effective prediction to be used in prognostic climate models. The previous attempts to measure CCN properties were limited to the regions close to Delhi (Bhattu et al., 2016; Jayachandran et al., 2020), and there are only a few studies investigating CCN properties in Delhi, which are however, based on, e.g., aerosol mass spectrometer and visibility data

(Arub et al., 2020; Y. Wang & Chen, 2019). This study reports aerosol hygroscopicity and CCN activity derived from size-resolved CCN measurements inside the metropolitan area of Delhi. The observations of CCN number concentrations are used as a proxy to understand aerosol–water vapour interaction, which governs the hygroscopic properties of aerosols in the atmosphere and therefore influences air quality and climate change (Z. Wu et al., 2018).

The topographical features and meteorological processes in Delhi are different from those of other megacities around the world. For example, the shallow PBL during winter in Delhi is typically caused by surface radiative cooling (Dumka et al., 2019; Ojha et al., 2020; Raatikainen et al., 2011; Tiwari et al., 2013) unlike in other megacities. Therefore, to capture the nuanced interaction of aerosols with atmospheric water vapour, which leads to cloud, fog and haze formation, visibility deterioration and health impacts, field measurements are essential. At present, we have a fair understanding of CCN activity from size-resolved CCN measurements under diverse environmental conditions (Schmale et al., 2018). This includes the clean Amazonian rainforest (Gunthe et al., 2009; Pöhlker et al., 2016, 2018), the coastal background site, Mace Head (Paramonov et al., 2015), and highly polluted megacities like Beijing (Gunthe et al., 2011) and Guangzhou (Rose et al., 2010, 2011) in China. Other locations where measurements are reported include the Thuringian forest in Germany (Henning et al., 2014), the coastal region in California (Asa-Awuku et al., 2015), the continental city of Kanpur in India (Bhattu et al., 2016), a peninsular region in Japan (Iwamoto et al., 2016), the South China Sea (Atwood et al., 2017), and the Yangtze River delta in China (Che et al., 2017; Ma et al., 2017). Here we present a comprehensive study of aerosols using size-resolved CCN measurements, supplemented by concomitant non-refractory PM1 (NR-PM1) composition and black carbon (BC) observations conducted within the metropolitan area of Delhi. From the 27-day-long campaign in Feb and Mar 2018, we investigated and identified the meteorological factors playing a major role in transforming aerosol chemistry, and retrieved CCN activity parameterizations validated against field measurements. During this short period, we observed two contrasting meteorological conditions characterized by the extent of radiative thermal inversion, which are in the following termed strong and weak inversion periods for the ease of reading. The resulting contrast in PBL height revealed interesting insights into the interaction of aerosols with water vapour, leading to cloud activation within the confined atmosphere of Delhi under varied anthropogenic emissions.

Previous studies on atmospheric aerosols in general, but not related to CCN, in Delhi have reported that primary sources of NR-PM1 such as biomass burning (BB) and fossil fuel combustion (Arub et al., 2020) are dominant in the overall PM mass burden, along with a major contribution from secondary aerosol formation all year round (Gani et al., 2019; Jaiprakash et al., 2017). Episodic peaks in primary organic aerosols along with ammonium chloride were reported previously by Gani et al. (2019) and Bhandari et al. (2020), as well as the companion study by Gunthe et al. (2021). Studies on the influence of meteorology on aerosol properties show that under uniform and unchanged sources of emissions, the extreme lowering of the PBL below 100 m during winters builds up extreme particulate matter concentrations, driving the Air Quality Index to hazardous levels (Bhandari et al., 2020; Dumka et al., 2019; Gani et al., 2019; Mandal et al., 2014; Murthy et al., 2020; Ojha et al., 2020). The influence of air mass history has also been reported in Delhi using back trajectory analysis (Arub et al., 2020; Jaiprakash et al., 2017). A comprehensive analysis provided in this study combining remote sensing and modelling approaches with measurements of CCN activity at eleven different supersaturations is unprecedented.

2 Methods and supplementary analysis

2.1 Measurement site, local meteorology, and experimental setup

Simultaneous measurements of size-resolved CCN, chemical composition of non-refractory PM1 (NR-PM1), and black carbon mass concentration were conducted as part of the Atmospheric

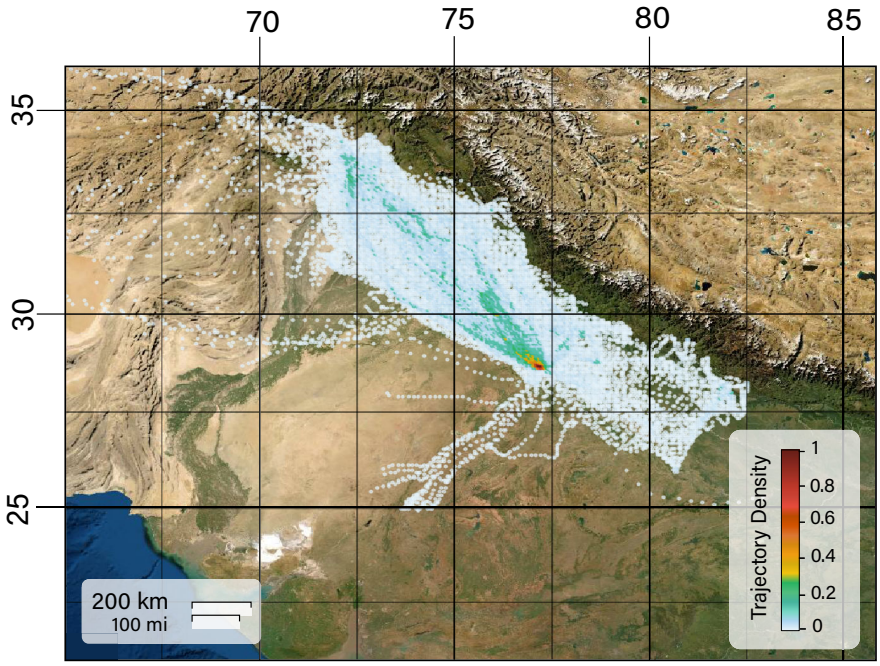

Figure 1. Three days of backward air mass trajectories estimated during the campaign period (Feb-Mar 2018), colour-scaled by the trajectory density with a resolution of 0.1°x 0.1°grid. A trajectory density of 1 indicates all sampled air masses passed through the indicated location. The map layer used is retrieved from ESRI (https:// services.arcgisonline.com/ ArcGIS/ rest/ services/ World Imagery/ MapServer/ tile/ z/ y/ x).

Pollution and Human Health Program under Process Analysis, Observations and Modelling – Integrated Solutions for Cleaner Air for Delhi (APHH – PROMOTE) field campaign. The field campaign was conducted towards the end of winter, from 05 Feb to 02 Mar 2018, and the measurement site was situated inside the campus of the India Meteorological Department, Delhi (28.5886°N, 77.2219°E; 214 m a.s.l., Fig. 1), located amidst the metropolitan area. Delhi is enclosed by the Thar desert (Rajasthan) to the west, the Deccan plateau to the south, and is located in front of the Himalayan mountain range, which extends from the north of Delhi to the far north east. The metropolitan area of Delhi is an extensively built-up area accommodating numerous small and large industries and transportation facilities, including a busy international airport, which is at a distance of ∼10 km (Guttikunda & Calori, 2013; Jain et al., 2016) from the campaign location.

The climate of Delhi is semi-arid with very hot summers, moderate monsoon, and cold winters. The winter is from early November to mid-February, characterized by cool days and cold and humid nights resulting in a distinct radiative thermal inversion (Arun et al., 2018; Dumka et al., 2019; Kumar et al., 2017; Ojha et al., 2020; Raatikainen et al., 2011; Thomas et al., 2019). The average diurnal temperature (T) cycled between 10 and 25 °C and the average diurnal RH from 26 to 90 %. In the present study we used the wind data collected at the Central Pollution Control Board (CPCB) operated station in Jawaharlal Nehru Stadium, which is at a distance of less than 1.5 km from the campaign location. The meteorological data at the CPCB site showed a strong correlation (R^2 >0.97; see Supplement Figure S1 and S2) with the quasi-continuous data measured at the observation site. Therefore, as the wind data from the CPCB site is continuously available, we used those in the present study and for all analysis requiring wind data.

The aerosol measurement instruments were placed in an air-conditioned container, fitted with a stainless-steel inlet ∼5 m above the ground. The inlet tubing was smoothly bent so that the cover of the meshed opening was upside down to bar the entry of rainwater and other debris. The aerosol samples were dried so that the moisture content was below ∼25 % *RH* using a diffusion drier containing silica gel (Merck, Germany; ∼1 - 3 mm size). Thereafter the polydisperse aerosol flow was divided using a 'Y'-shaped splitter and used to supply (i) an aerosol number size distribution and size-resolved CCN setup; and (ii) a chemical composition measurement setup. The temperature inside the container was maintained at ∼28 °C throughout the campaign to ensure a stable working environment for the instruments.

2.2 Back trajectory and fire spot analysis

The spatiotemporal pattern of air masses over Delhi was studied using 3-day back trajectory (BT) data, retrieved using the HYSPLIT (The Hybrid Single-Particle Lagrangian Integrated Trajectory) model (Stein et al., 2015). A fixed height of 1000 m above the ground was used as top of the model for the analysis. Three years of data (1 Jan 2016 to 31 Dec 2018), which constituted 26304 BTs, with each BT containing 73 latitude-longitude data pairs were clustered spatially using the Quickbundles algorithm (Garyfallidis et al., 2012) in Python (Van Rossum & Drake, 2009). It is a fast clustering method, for simplifying complex and large sets of tractography data. Quickbundles has a built-in metric called the minimum average direct-flip distance (MDF), which selects the minimum among the Euclidean distance between trajectories determined using two methods, one that considers points that lie in the same sequential position and another that considers points lying in opposite sequence in both trajectories. MDF efficiently separates the BTs based on length as well as direction. Based on this algorithm and subsequent analysis results, we identified nine major BT cluster directions in a year. Out of this, only three could be mapped for the time of the year we conducted the measurements. They were north-west (NW), south-east (SE) and mixed regional pollution (MRP).

The most frequently sampled air mass during the campaign belonged to NW, which gave us 540 samples in the size-resolved CCN experiment (or CCN scans), followed by MRP which gave 149 scans, and SE which gave 44 scans, out of the total 733 good-quality CCN scans. The density of BTs in a grid of 0.1°x 0.1°was also calculated and plotted (Fig.1) using a program written in Python. To complement the BT analysis, fire intensity ($W\,m^{-2}$) maps were retrieved from Copernicus Atmosphere Monitoring Service (CAMS) - Global Fire Assimilation System (GFAS). The data were in NetCDF3 format and the graphs were visualized in QGIS overlaid on a geo-referenced map layer of India. During the measurement period, the fire spot data analysis revealed a series of small fire events much farther than the consistent fire spots present over Punjab and Haryana, which generally affect air quality in Delhi during the stubble burning period of Oct-Nov. Our fire spot analysis further confirms the presence of fire spots in Oct and Nov-2017 preceding our campaign.

2.3 Planetary boundary layer modelling

The Weather Research and Forecasting model (WRF version 4.0) was used to simulate diurnal variation in planetary boundary layer height (H_{BL}). The centre of the model domain is at 76°E, 29°N, and there are 240 grid points in the east-west direction and 147 grid points in the north-south direction on a Mercator projection, along with 51 vertical levels. Model simulations are conducted at a resolution of 12 km x 12 km. Initial and lateral boundary conditions for the meteorological fields were prepared using the Era Interim data (https:// www.ecmwf.int/ en/ forecasts/ datasets/ reanalysis-datasets/ era-interim). Model simulation was conducted for the period of 28 Jan 2018 to 3 Mar 2018 at a time step of 72 s and the model output was stored every hour for analysis. The first 4 days of model output have been discarded to account for model spin-up. Physics schemes used in the model to parametrize different processes were: i) Lin et al. scheme for cloud microphysics; ii)

Grell 3D ensemble scheme for cumulus parameterization; iii) Unified Noah land surface model for land surface option; iv) Rapid radiative transfer model for long wave radiation and v) Goddard shortwave scheme for short wave radiation. Two PBL schemes were used in two different simulations: i) Mellor-Yamada-Janjic scheme (representing the turbulence kinetic energy) and ii) Yoinsei University scheme (based on Bulk Richardson number).

We also analyzed the latest ECMWF satellite reanalysis data set, ERA5, and the mixing depth from HYSPLIT model for the same period. On comparison of the above data sets with the quasi-continuous ceilometer measurements carried out at the same location as part of this campaign (Murthy et al., 2020), the WRF modelled results and ERA5 data showed good correlation (Figure S3 and S4, Table S1). However, the WRF modelled data with the Bulk Richardson number method was used in this study, considering the finer spatial resolution compared to ERA5 (0.5°x 0.5°). This data is provided in the supporting dataset.

3 Instrumentation and data analysis

3.1 Size-resolved CCN measurements

The size-resolved CCN measurements were carried out based on Frank et al. (2006) and Rose et al. (2008), by the coordinated controlling of three instruments, viz., a Cloud Condensation Nuclei Counter (CCNC, model CCN-100, DMT; Roberts and Nenes (2005)) to determine CCN number concentration, an electrostatic classifier (EC, model 3080, TSI) with a differential mobility analyzer (long DMA, model 3081, TSI) to select monodisperse aerosol particles, and a condensation particle counter (UCPC, model 3776, TSI) to count total aerosol particles. The entire setup was controlled externally by a computer which runs a dedicated, in-house developed, and well tested LabVIEW (National Instruments, Munich, Germany) program (Pöhlker et al., 2016) to continuously sample ambient aerosols of the size range relevant to cloud processing (26 size bins or mobility diameters (D) in the range, 10 to 370 nm) and measure cloud droplet activation at different supersaturation (S) levels.

The dried polydisperse aerosol samples were drawn into the EC through an inertial impactor that prevents particles larger than ∼370 nm from entering the system. Inside the EC, the polydisperse aerosol flow was passed through a radioactive neutralizer (Kr-85, model 3077A, TSI) to attain a known charge distribution. The charged particles were then passed through an electric field inside the long-DMA, where they were segregated based on their electrical mobility. The DMA was controlled by the LabVIEW program to set the appropriate voltage in order to select the desired D and produce a near-monodisperse aerosol flow. This flow was further split, using a 'Y'- shaped connector tube, between CCNC and UCPC to measure CCN and total aerosol number concentration for the chosen diameter. The DMA maintained the near-monodisperse flow of selected D for 30 s, then switched to the next D after flushing out the DMA column for 40 s to make it particle-free. Meanwhile, the CCNC was controlled to maintain a specific S level for a duration of 40 min, to let all the successive D steps pass through the instruments. The CCNC measured the particles of D activated as cloud droplets ($N_{\mathrm{CCN}}(S,D)$) employing the empirical approach of counting the droplets greater than 1 μm (Roberts & Nenes, 2005; Rose et al., 2008) at the S level attained inside the CCNC column. This method was adopted since larger particles are not sampled and therefore the probability of counting unactivated particles as CCN was low (Y. Wang et al., 2019). Simultaneously, the UCPC measured the total particle number concentration for a given D ($N_{\mathrm{CN}}(D)$). A relevant set of 11 selected S levels were cycled in the CCNC column by providing an equilibration time of 5 min between each S, taking ∼8 hrs to finish a complete cycle of S levels.

The sample flow through the DMA was 0.8 L min^{-1}, which includes the 0.3 L min^{-1} to the UCPC and 0.5 L min^{-1} to the CCNC. The sheath to sample flow ratio inside the DMA was 7.5, and the total flow to aerosol flow ratio inside the CCNC was 10. The liquid supply pump was working in the low flow mode with a supply of 4 mL h^{-1}. The size-resolved

CCN experiment setup measured aerosol samples at temperature 299 ± 2.3 K, pressure 959 ± 8.2 hPa, and $25\,\% \pm 5\,\%$ *RH* (arithmetic mean $\pm$ standard deviation).

The CCNC was systematically calibrated based on Rose et al. (2008) for different S levels before and after the 27-day campaign (02 Feb and 03 Mar 2018). Calibrations were performed using standard ammonium sulphate aerosols, whose cloud droplet activation is well explained using classic Köhler theory. Standard ammonium sulphate aerosols were generated by nebulizing an aqueous salt solution ($0.3\,\mathrm{g\,L^{-1}}$) of ammonium sulphate ($(NH_4)_2SO_4$, purity >99.5 %) in a TSI Aerosol Generator. Both calibration experiments gave a similar relationship between the S level estimated experimentally (or effective supersaturation, S_{eff}) and the corresponding measured temperature gradient ($\mathrm{d}T$, K) inside the CCNC column. This ensured the stable functioning of the CCNC during the campaign period. All S levels for which parameters are reported in this paper refer to experimentally derived S_{eff}.

3.2 Measurement specifications

It should be noted that the measurements made in the study are not strictly ambient, due to the conditioning of the aerosol samples taken from the atmosphere to a moisture content below 25 % *RH*. It is strongly possible that there are losses of volatile species during the passage of the air through the chambers of the various instruments, which are operated at a fixed temperature. Nevertheless, the measurements reported should be considered as the intrinsic properties of aerosols at the following atmospheric conditions, $T = 299 \pm 2.3$ K, $P = 959 \pm 8.2$ hPa and $RH = 25\,\% \pm 5\,\%$ (arithmetic mean $\pm$ standard deviation measured during campaign). To convert to standard conditions (STP: 273 K, 1000 hPa, 0 % *RH*), the reported values can be multiplied by a factor of 1.08 (derived using the ideal gas law). However, this correction does not account for the change in particle size, mass and hygroscopicity due to loss of volatile species, interaction with gaseous phase components, and gas - particle partitioning.

3.3 Data analysis of size-resolved CCN measurements

Size-resolved CCN measurements provide the cloud activated fraction ($N_{\mathrm{CCN}}(S,D)/N_{\mathrm{CN}}$) for a selected D at the S level attained in the CCNC column. The values of $N_{\mathrm{CCN}}(S,D)/N_{\mathrm{CN}}$ plotted against the corresponding D for the entire particle size range sampled at a single measured S level gives a CCN activation curve, which constitutes a measured scan. The average CCN activation curves measured at each S level are shown in Figure 2. The most important parameter obtained from these curves is the midpoint activation diameter ($D_{\mathrm{a}}(S)$), which is the minimum diameter required for activation of 50 % of condensation particles in the sample at given S level. Over the course of the entire campaign, 744 scans of entire particle size range at a single S level were measured and analyzed to calculate CCN properties based on the theories put forth in Petters and Kreidenweis (2007) and Rose et al. (2008). Based on the quality of data, 733 scans (Raj et al., 2021) were selected for further analyses and representation in this study.

3.4 Errors and corrections in size-resolved CCN data

Practical limitations of the instruments generally introduce errors in the measured mobility diameter of particles and activated fractions. The outlet slit of the DMA has a finite width and hence it permits a size bin, rather than a fixed size in the outflow (Knutson & Whitby, 1975). Moreover, some of these particles carry multiple charges and attain enhanced electrical mobility inside the DMA. These multiple-charged particles flow along with smaller single-charged particles of similar electrical mobility resulting in enhanced activated ratios and induce errors. The measured activated fractions were corrected for multiple-charged particles based on Frank et al. (2006), by taking into account the presence of up to quadruple-charged particles. Following Rose et al. (2008) these corrected fractions

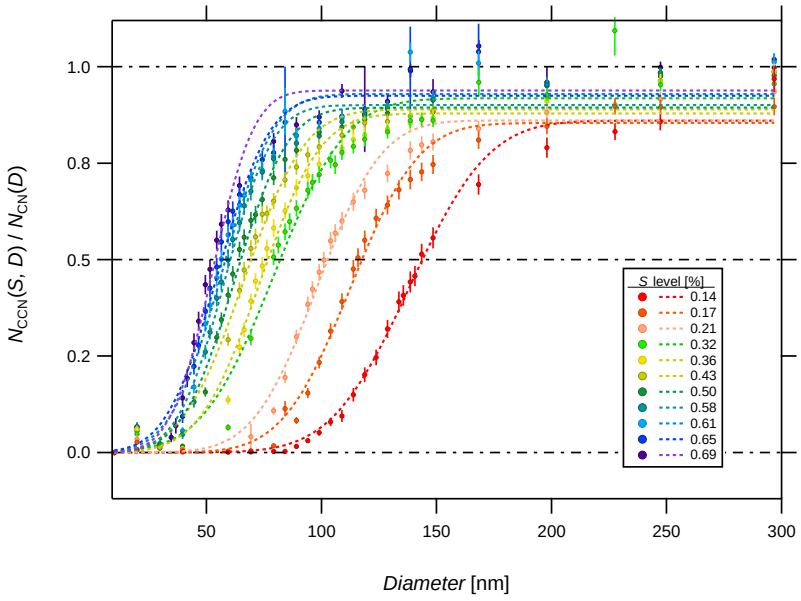

Figure 2. Average CCN activation across selected size bins for all measured S levels during the campaign. The error bars indicate standard error for observations in each size bin at each S level. The dashed lines are the single-erf fit based on Rose et al. (2008)

were used to back-calculate the measured diameter by applying the transfer function, which is the probability of a certain D passing through the DMA's slit (Knutson & Whitby, 1975). The corrected activation curves were fitted with a 3-parameter cumulative distribution function (CDF) using the non-linear least squares fitting routine (Gauss-Newton method, Matlab, MathWorks, Inc.) defined by the parameters: $D_a(S)$; $N_{CCN}(S,D)/N_{CN}$ at 50 % activation or $a(S,D)$; and the width of the activation curve or $\sigma(S)$ (Rose et al., 2008).

3.5 Size data inversion for particle number size distribution

Due to instrumental limitations the routinely measured aerosol particle number size distribution could not be used for further analysis. Therefore, alternatively we used the aerosol number size distribution obtained by the inversion of $N_{CN}(D)$ data retrieved during size-resolved CCN measurements. A dedicated inversion routine was developed (Matlab, MathWorks, Inc.) following the method and approximations described by Wiedensohler (1988).

The measured $N_{CN}(D)$ is the concentration of particles in a narrow size bin, D, governed by the electrical mobility of the particles inside the DMA. Since the DMA used had a negatively charged electrode, $N_{CN}(D)$ was the concentration of only the positively charged particles. Moreover, the UCPC measures only half the original concentration of positively charged particles, owing to the triangular nature of the transfer function (Knutson & Whitby, 1975). Hence two times the value of $N_{CN}(D)$ is used to account for this loss. The inertial impactor at the sampling inlet of DMA ensures that only those particles less than a given cut diameter enter the instruments, and the largest size bin (D_{max}) sampled was approximately equal to this cut diameter. Therefore, the concentration at D_{max}, $N_{CN}(D_{max})$ corresponds to only +1 charged particles, so it required no multiple charge correction.

In order to calculate near-ambient particle concentrations, the measured 2^*N_{CN} values are divided by the probability of the radioactive neutralizer generating particles

of charge e = +1 in each D (Wiedensohler, 1988). This quantity, when calculated for all D except $D_{\max}$, includes particles carrying multiple charges in the range, e = [-4, +4]. So the multiple charge correction is applied for up to 2 charges using Wiedensohler's coefficients (Wiedensohler, 1988) and for 3 to 4 charges using Gunn's equation (Gunn, 1954).

The inverted size distribution was compared with quasi-continuous parallel measurements of aerosol number size distribution using an SMPS consisting of an electrostatic classifier (EC, model 3082, TSI) with Nano DMA (model 3085, TSI) and a condensation particle counter (CPC, model 3772, TSI). Although the measured size range of the Nano-SMPS was 8 to 105 nm, it served as a quality check for the inverted particle concentration in that size range. The qualitative match of the inverted size distribution was in good agreement, with about a 23.1 % reduction in number, which is expected due to the size-resolved mode of measurement, where the mobility diameter was selected step-wise unlike the continuous scanning mode done in the SMPS. Hence in order to take this loss into account, the inverted particle number size distribution ($\mathrm{d}N/\mathrm{dlog}D$) and particle concentrations in the size range 10 to 370 nm ($N_{\mathrm{CN},10}$) reported in this paper have been up-scaled by a factor of 1.3 (Raj et al., 2021).

S [%]	$D_{\mathrm{a}}(S)$ [nm]	$\kappa(S,\ D_a)$	$\sigma(S)$ [nm]	$MAF(S)$	$N_{\mathrm{CCN}}(S)$ [cm^{-3}]	$N_{\mathrm{CN},10}$ [cm^{-3}]	$N_{\mathrm{CCN}}(S)/N_{\mathrm{CN},10}$	n
0.14	141 ± 14	0.28 ± 0.09	26 ± 9	0.85 ± 0.16	4341 ± 2607	17789 ± 9460	0.26 ± 0.10	65
0.17	115 ± 10	0.31 ± 0.08	23 ± 8	0.86 ± 0.16	5959 ± 3268	16550 ± 8414	0.37 ± 0.12	70
0.21	101 ± 9	0.31 ± 0.08	25 ± 10	0.89 ± 0.14	7230 ± 3883	16772 ± 8708	0.45 ± 0.13	69
0.32	80 ± 7	0.27 ± 0.07	22 ± 8	0.90 ± 0.12	9143 ± 5136	16861 ± 9213	0.55 ± 0.12	67
0.36	75 ± 8	0.27 ± 0.09	20 ± 10	0.90 ± 0.13	10149 ± 5839	17592 ± 9571	0.59 ± 0.12	67
0.43	68 ± 7	0.25 ± 0.07	21 ± 7	0.91 ± 0.13	10800 ± 6148	17672 ± 9449	0.62 ± 0.14	64
0.50	64 ± 7	0.22 ± 0.07	18 ± 9	0.91 ± 0.12	11721 ± 6708	18117 ± 9371	0.65 ± 0.13	63
0.58	60 ± 8	0.21 ± 0.10	18 ± 8	0.92 ± 0.12	12277 ± 7497	18100 ± 9796	0.68 ± 0.13	65
0.61	58 ± 8	0.20 ± 0.08	19 ± 10	0.92 ± 0.12	12493 ± 6987	18492 ± 9268	0.68 ± 0.14	64
0.65	56 ± 8	0.20 ± 0.10	17 ± 8	0.92 ± 0.12	12959 ± 6620	18941 ± 9218	0.70 ± 0.13	62
0.69	54 ± 8	0.20 ± 0.11	15 ± 8	0.94 ± 0.10	13252 ± 7147	18486 ± 8920	0.72 ± 0.12	65

Table 1: CCN properties measured during Feb - Mar 2018 at Delhi shown as a function of effective supersaturation achieved inside the CCNC. The S levels are average values measured with a standard deviation of ∼0.001 %. All other values are expressed as average ± standard deviation. Parameters tabulated are: midpoint activation diameter ($D_{\mathrm{a}}(S)$), hygroscopicity from size-resolved CCN measurements ($\kappa(S,\ D_a)$), width of the CCN activation curve ($\sigma(S)$), maximum activated fraction ($MAF(S)$), total CCN concentration ($N_{\mathrm{CCN}}(S)$), total particle concentration in the size range ∼10 to 370 nm ($N_{\mathrm{CN},10}$), CCN efficiency ($N_{\mathrm{CCN}}(S)/N_{\mathrm{CN},10}$), and number of samples for each S level (n).

3.6 CCN properties

The parameters of the CDF fit to the activation curves, along with S_{eff} and particle number size distribution were used to calculate key CCN properties (as enumerated below) based on literature.

1. Effective hygroscopicity parameter of the aerosol population: $\kappa(S,D_{\mathrm{a}})$
   The measured $D_{\mathrm{a}}(S)$ and corresponding S_{eff} were used in κ-Köhler theory (Petters & Kreidenweis, 2007) to calculate the effective hygroscopicity parameter $\kappa(S,D_{\mathrm{a}})$, which encompasses all the composition dependent variables (Atwood et al., 2017; Gunthe et al., 2009; Pöhlker et al., 2016; Rose et al., 2008).
2. Maximum activated fraction of the aerosol population at S: $MAF(S)$
   The fit parameter of CDF, $a(S,D)$ gives the ratio of CCN to CN particles at S when 50 % activation has occurred. From this, MAF is calculated as $2^{*}a(S,D)$. If less

than 100 % of the aerosol population is activated, MAF will be less than 1 and indicates the presence of externally mixed CCN inactive particles (Gunthe et al., 2009; Pöhlker et al., 2016; Rose et al., 2008).

3. Total number concentration of CCN at S: $N_{\mathrm{CCN}}(S)$
   The measured CN distribution was multiplied by the corresponding activation curve or CDF at given S to obtain the CCN distribution. Then, total CCN is calculated by integrating the particles under the CCN number size distribution (Gunthe et al., 2009; Pöhlker et al., 2016; Rose et al., 2008).
4. CCN efficiency of the aerosol population at S: $N_{\mathrm{CCN}}(S)/N_{\mathrm{CN}}$
   The ratio of total CCN number concentration at a given S to the corresponding total CN number concentration gives the CCN efficiency of the sampled aerosol population (Gunthe et al., 2009; Pöhlker et al., 2016; Rose et al., 2008).

Average CCN properties measured during the field campaign are tabulated as a function of experimentally derived S levels in Table 1. Since the time taken for measuring a complete set of S levels was long (∼8 hrs), we have examined the frequency of measurements of all S levels in a full diurnal cycle for the entire data, to assess the impacts on CCN measurements. The distribution was similar, indicating that the CCN properties reported are not biased towards a period in the diurnal cycle for the S levels and therefore, the CCN measurements are not much affected by the long time taken by one complete S cycle.

3.7 Aerosol chemical composition and black carbon measurements

Simultaneous measurements of non-refractory PM1 (NR-PM1) aerosols were carried out using an Aerosol Chemical Speciation Monitor (ACSM), which uses a quadrupole mass spectrometer (Ng et al., 2011). The calibration and measurement technique of this instrument are explained in detail elsewhere (Gunthe et al., 2021).

Equivalent mass concentrations of BC ($M_{\mathrm{BC,e}}$) were measured using an Aethalometer (Model AE33, MAGEE Scientific). The instrument uses the optical absorption of aerosols at different wavelengths ranging from near infra-red to near ultraviolet to estimate the mass of BC. The reported $M_{\mathrm{BC,e}}$ corresponds to the optical absorption at 880 nm wavelength. Some of the results and other details of the chemical composition data from these measurements are also reported in Gunthe et al. (2021) and Reyes-Villegas et al. (2021).

4 Results and Discussion

The temporal evolution of the measured characteristic aerosol and CCN properties, meteorological parameters and modelled results are shown in Figure 3. The top strip of the compendium plot shows the 3-day back trajectory analysis of sampled air masses, using the HYSPLIT model (Stein et al., 2015)(see Section 2.2). It marks the duration of occurrence of three distinct directions derived using the HYSPLIT model indicating the origin and path of the air mass: north-west (NW), south-east (SE), and mixed regional pollution (MRP) consisting of both, north-west and south-east branches. Panel (a) shows the wind speed colour-scaled by the wind direction (see Section 2.1), indicating the occurrence of low wind speed (<5 $\mathrm{m\,s^{-1}}$) during this season on local scale. The wind speed exhibited a systematic diurnal cycle with lower wind speeds (<3 $\mathrm{m\,s^{-1}}$) during the nighttime and relatively faster wind during the daytime. The wind direction did not display any diurnal pattern, potentially indicating the influence of surface roughness (Jacobson et al., 2019) on winds in Delhi. The temperature and relative humidity (T and RH, Fig. 3b) cycles diurnally with high T and low RH during the daytime, particularly at late afternoon hours. The PBL height (H_{BL}) simulated using the WRF model (see Section 2.3) is shown in panel (c). The alternating occurrence of low wind speed, low T and high RH during the nighttime contributed to a shallow nocturnal PBL, resulting in pronounced diurnal variations in H_{BL}.

A strong influence of the shallow nocturnal boundary layer was observed on the measured aerosol mass and number concentrations (Fig. 3c and 3d). To further investigate

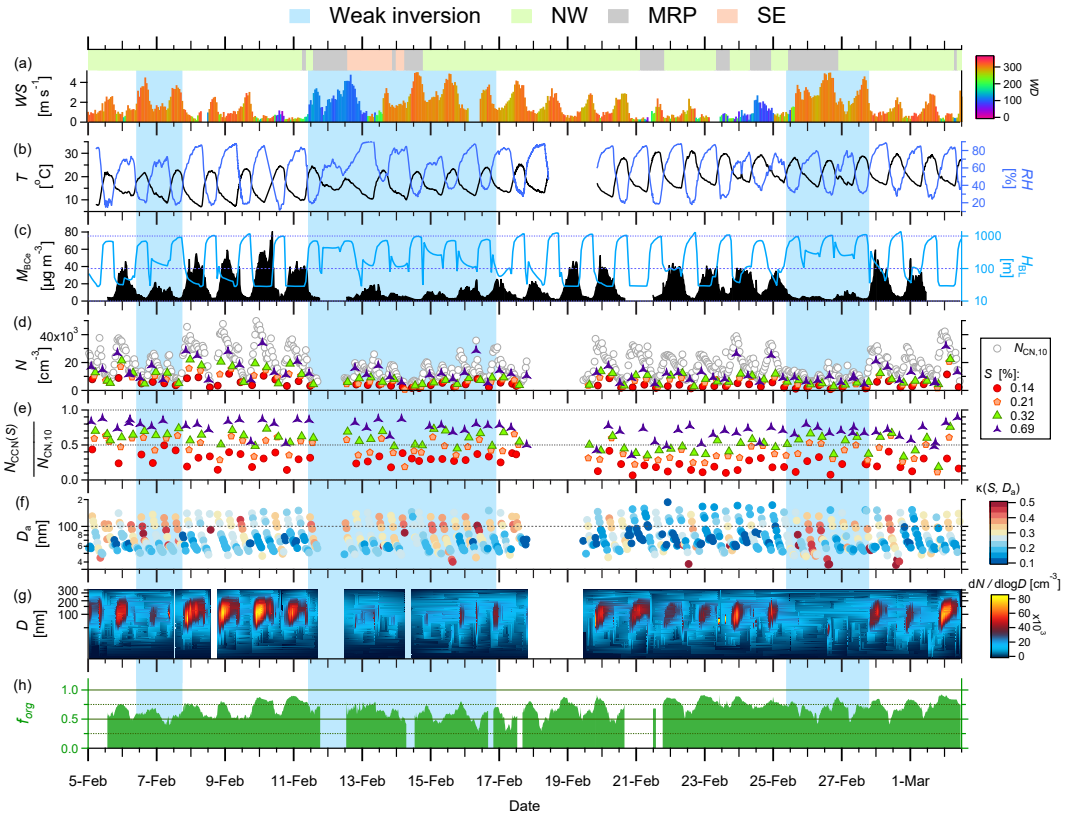

Figure 3. Evolution of meteorological and aerosol parameters shown as a function of local time. Strong radiative inversion periods and weak radiative inversion periods are indicated by white and blue graph background, respectively. The shading on top indicates the air mass observed: north-west (green); south-east (orange) and mixed regional pollution (grey). Temporal evolution of (a): Wind speed (WS, m s^{-1}) colour-scaled by wind direction (WD, degrees); (b): Temperature (T, °C) on the left axis, and relative humidity (RH, %) on the right axis; (c): Mass concentration of equivalent BC ($M_{\mathrm{BC,e}}$, μg m^{-3}) on the left axis, and planetary boundary layer height (H_{BL}, m) from the WRF model on the right axis; (d): Total particle number concentration in the size range ~10 to 370 nm ($N_{\mathrm{CN,10}}$, cm^{-3}), and CCN concentration at selected S levels (N_{CCN}(S), cm^{-3}); (e) CCN efficiency (N_{CCN}(S)/$N_{\mathrm{CN,10}}$) at selected S levels; (f): Hygroscopicity ($\kappa(S,D_a)$) is plotted as colour of dots against the midpoint activation diameter (D_{a}, nm) as y-axis. Larger D_{a} corresponds to lower supersaturation and vice versa; (g) Particle number size distribution (dN/dlog$D$, cm^{-3}) shown as a heat map from 10 to 370 nm; (h) Organic mass fraction of NR-PM1 (f_{org}).

the dependencies between the modelled H_{BL} and measured meteorological parameters and characteristic aerosol properties, the diurnal variations of H_{BL}, RH and T, along with the aerosol properties that show strong correlation to H_{BL} are shown in Figure 4. We found that the relations between H_{BL} and BC (M_{BCe}, see Fig. 4a and b), and the aerosol loading (see Fig. 4a and b) are the strongest at the diurnal scale. The average diurnal variation of the modelled H_{BL} (Fig. 4a) is in good agreement ($R^2 = 0.95$) with the observed ceilometer data measured at the same location and period as reported by Murthy et al. (2020). An increase in H_{BL} is observed after 08:00 LT (Local Time, i.e. UTC + 05:30) in the morning, corresponding to the rise in temperature and drop in RH. This indicates that the convective mixing after 08:00 LT leads to the breaking of the nocturnal

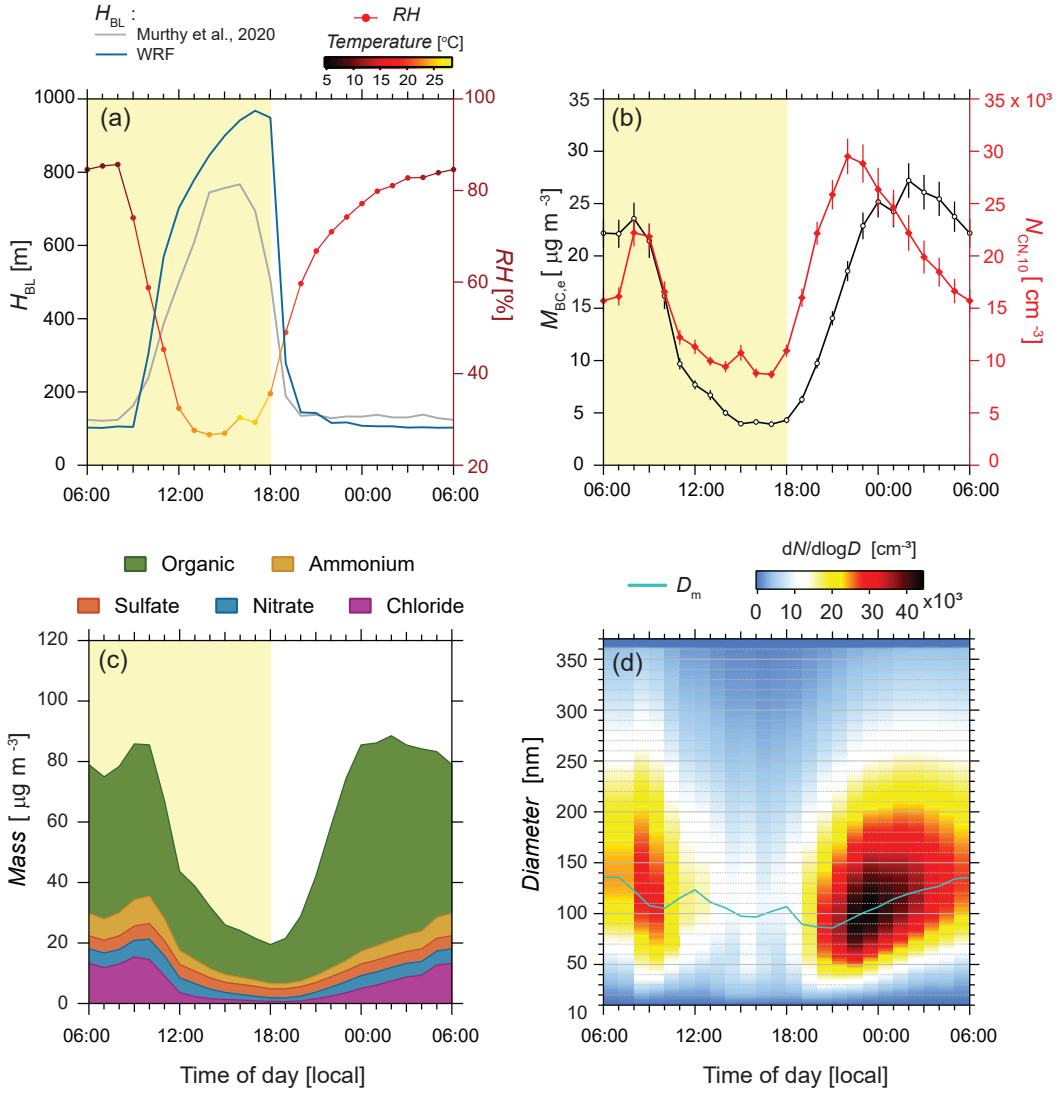

Figure 4. All panels show the campaign-average diurnal variation of the parameters. (a): Planetary boundary layer height (H_{BL}) modeled by the WRF model (blue) and measured by ceilometer from Murthy et al. (2020) (grey) (left axis). The relative humidity, colour scaled by the average diurnal atmospheric temperature, is plotted on the right axis. (b): Equivalent mass of BC ($M_{\mathrm{BC,e}}$) on the left axis and total particle concentration in the size range ∼10 to 370 nm ($N_{\mathrm{CN,10}}$) on the right axis. (c): Mass of NR-PM1 species, organic, ammonium, sulfate, nitrate and chloride from the ACSM as stacked plot. (d): Average size distribution in each hour as a heat map and the modal diameter (D_{m}).

stable layer, resulting in an increase in H_{BL}, which sustained until 18:00 LT. As night falls, the ground surface cools faster than the PBL air, causing a radiative inversion and resulting in the H_{BL} being close to the ground surface (Gopalakrishnan et al., 1998; Singh, 2016; Stull, 2012). Hence, the nocturnal atmosphere is static, stable, cold, and humid, and persisted for an extended duration during nighttime (∼18:00 LT to ∼08:00 LT).

The mass concentration of equivalent BC, the total particle number concentration (Fig. 4b), and the mass concentrations of the NR-PM1 chemical species (Fig. 4c) followed a similar trend, indicating a dominant contribution of locally emitted aerosol from sources

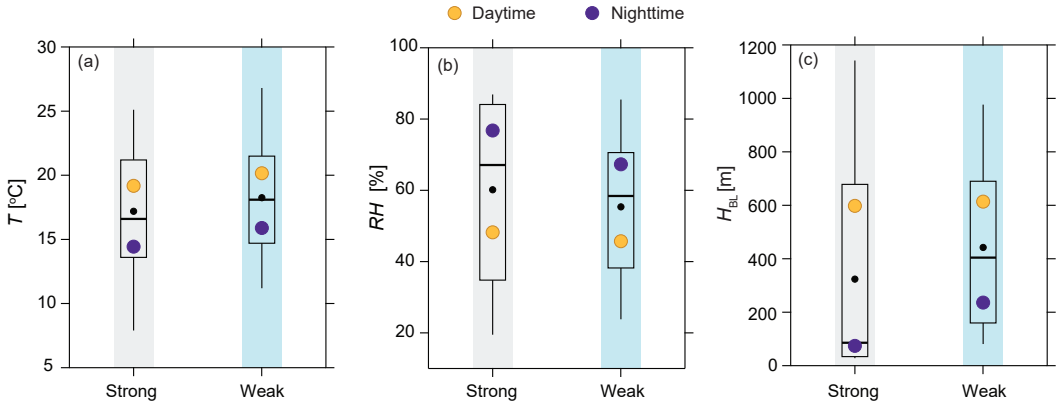

Figure 5. Quartiles and averages of meteorological parameters during strong and weak inversion periods (a): temperature, (b): relative humidity, and (c): planetary boundary layer height. The whiskers show 95th and 5th percentile values, black dots show the averages of data under the specified period and the other coloured dots show the averages of the data during the daytime and nighttime as given in the figure.

like fossil fuel combustion, solid biomass burning for domestic cooking and heating, burning of other waste materials, etc. to the total aerosol mass burden. All parameters consistently exhibited a characteristic morning rush hour peak between 06:00 LT and 09:00 LT, subsequently showing a drop thereafter. This drop strongly coincides with the PBL rise, and therefore is further pronounced due to dilution by convective mixing. The nighttime peak starts at 19:00 LT coinciding with the evening rush hour as well as the drop in H_{BL}, which results in the reduction of PBL mixing volume and facilitates enhanced nighttime concentration. While $N_{\mathrm{CN,10}}$ drastically decreased after the rush hour at 22:00 LT, indicating either particle removal or coagulation (to be discussed in follow-up studies), the BC and NR-PM1 mass concentrations continued to rise until 00:00 LT. The prominent late night BC peak has been attributed to diesel engine exhaust emissions from trucks and other heavy vehicles, which are permitted passage through Delhi only after 21:00 LT (Guttikunda & Gurjar, 2012). The mass concentrations of organic and major inorganic components also followed the typical diurnal trend in concentration variations (Fig. 4c). These observations are consistent with the diurnal trend of PM1 concentrations previously reported by Gani et al. (2019) in Delhi. The average diurnal cycling of aerosol number size distribution (Fig. 4d) further shows that the dominant size range of aerosol particles emitted during the morning and evening rush hours consistently remained in the range of 80 nm to 100 nm. It is interesting to note that a growth in particle modal diameter from ∼80 nm to ∼140 nm was observed starting in the evening hours (18:00 LT) and lasting until almost early morning (06:00 LT), consistent with the observations reported by Gani et al. (2020). The detailed processes and mechanisms with possible implications of such a growth will be discussed in a follow-up study.

Although the average diurnal cycling of H_{BL} was pronounced, a closer look at panel (c) in Fig. 3 reveals multiple periods with weak diurnal cycling of H_{BL}. These periods of weak diurnal cycling coincided with a low solar radiation, and a reduced difference between the maximum and minimum temperature during the following diurnal cycle (Figure S5; see Text S1). Low solar radiation can cause relatively faster radiative cooling of the atmosphere when night falls, which leads to increase in nighttime H_{BL}, resulting in a more ventilated nocturnal atmosphere (Stull, 2012). These periods were classified as weak inversion periods (blue background in Fig. 3; see Table S2 for time of occurrence). The rest of the campaign, with stronger solar radiation, were classified as strong inversion

periods (white background in Fig. 3; see Table S2 for time of occurrence). The strong inversion periods were marked with higher near-surface RH levels during the nighttime as shown in Figure 5b. Since moist air is characterized by higher heat transfer (Still et al., 1998), this could cause warming of the atmosphere above ground, which would result in reduced inversion layer thickness (Pasricha et al., 2003) and hence, could induce a positive feedback to lowering of H_{BL}. The above observations were substantiated by the PBL simulations that showed lower nighttime H_{BL} during strong inversion periods in contrast to the higher nighttime H_{BL} during weak inversion periods (Fig. 5c; see Text S1). Overall, the statistical properties of RH and H_{BL} were different during nighttime between strong and weak inversion periods, whereas they were comparable during daytime for both periods.

To better understand the role of meteorology on aerosol extensive and intensive properties and their interdependence, we plotted real-time $N_{\mathrm{CN,10}}$ values against H_{BL} for strong and weak inversion periods. We further scaled it by wind direction and speed, and RH (Figure 6). Based on the minimum, maximum and quartile values, the H_{BL} was divided into four classes (28 m to 50 m, 50 m to 158 m, 158 m to 685 m, and 685 m to 1374 m). The categorization of observations and naming of each class (see top strip of Fig. 6) was done based on the probability of occurrence of nighttime observations during strong inversion periods (further referred to as 'strong inversion-nighttime'), nighttime observations under weak inversion period (further referred to as 'weak inversion-nighttime') and daytime observations in each inversion periods (Table S3). The transition class (H_{BL} = 50 m to 158 m) exhibited a similar probability of occurrence of both strong and weak inversion-nighttime. Since H_{BL} values during daytime of both strong and weak inversion periods did not exhibit any difference, they were merged into a single class, daytime. Only the first class (H_{BL} = 28 m to 50 m), which has the smallest PBL mixing volume and the lowest wind speeds, showed high $N_{\mathrm{CN,10}}$. This class accommodated 60% of the observations during strong inversion-nighttime, while only 5 % of weak inversion-nighttime and 9 % of daytime observations fall in this class. Hence, strong inversion-nighttime is characterized by a shallow, stable and static boundary layer with enhanced aerosol concentration close to the ground. Faster winds contributing to dilution and hence low $N_{\mathrm{CN,10}}$ are observed mostly during the weak inversion-nighttime periods, and the daytime periods irrespective of the different inversion strength. During strong inversion-nighttime however, the faster winds caused lower $N_{\mathrm{CN,10}}$ as shown in Fig. 6a.

As expected, the wind direction does not show any trend during the different inversion conditions (Fig. 6b), indicating that the contributions to total aerosol burden were dominated by local city emissions over any long range transported aerosols. Further, the high number concentration resulting from stagnant and local winds during strong inversion-nighttime with high RH (Fig. 6c) can facilitate the multiphase processes and heterogeneous reactions leading to formation of secondary aerosols affecting the aerosol hygroscopicity (Gunthe et al., 2021). Hence, such an overall scenario can not only affect the extensive properties of the aerosols (higher aerosol mass burden associated with stagnant and local winds) but can also under favourably high RH conditions modulate the intensive aerosol properties. The above observations suggest that aerosol concentrations drastically increase only under low H_{BL} during nighttime characterized by low wind speeds and high RH caused by the preceding lower solar radiation, and therefore, highlights the influence of local meteorology on aerosol properties. The dependency observed in this study between H_{BL} and aerosol number and mass concentration is in good agreement with previous studies reporting aerosol properties over Delhi (Bhandari et al., 2020; Gani et al., 2019, 2020).

In contrast to previous studies, however, we found no correlation between the air mass origin and aerosol properties for the period we performed the measurements. The HYSPLIT model simulation of BTs using a constant height of 1000 m as top of the model showed that majority of the BTs belonged to the NW air mass consisting of longer trajectories and brief periods of MRP and SE air mass with shorter trajectories (Figure S6a, S6b and S6c). All three categories of air masses had overlapping paths in the proximity of the megacity. Since SE was observed for a shorter period and does not cover a complete cycle of S levels, only NW and MRP were used for further analysis. Aerosol populations measured

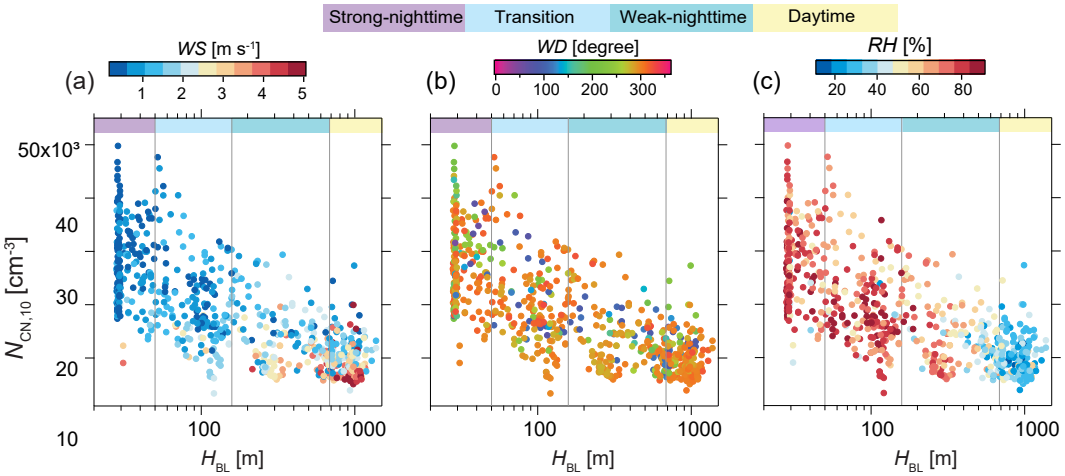

Figure 6. Correlation of H_{BL} with $N_{\mathrm{CN},10}$ colour-scaled by (a): wind speed (WS, $\mathrm{m\,s^{-1}}$), (b): wind direction (WD, degree) and (c): relative humidity (RH, %). Classification of measurements based on H_{BL} into classes, strong nighttime, transition, weak nighttime and daytime is indicated on top of each graph.

under a given air mass (both NW and MRP) did not show consistent diurnal trends of BC mass, aerosol and CCN number concentration during its period of occurrence (see Fig. 3 top strip, 3c and 3d); moreover, a reduction in concentration and changes in aerosol hygroscopicity were observed for a given air mass when weak inversion conditions overlapped with its occurrence (see Fig. 3 top strip, 3 blue graph background, 3c, 3d and 3f). The average aerosol number size distribution was qualitatively similar during NW, MRP and SE with NW alone exhibiting slightly higher number concentration. The average aerosol hygroscopicity distribution was also similar for NW, MRP and SE air masses (Figure S6). Further investigation of the trend in aerosol properties during the daytime and nighttime of the respective air masses showed that the average aerosol properties were different between daytime and nighttime only for NW air masses (Figure S7). This, however, cannot be attributed to the influence of the specific air mass, as the differences in aerosol properties between daytime and nighttime was discernible for NW air masses when they coincided with strong inversion periods (Figure S8a). This was consistent for MRP air masses as well (Fig. S8c). It should be noted that the frequency of strong inversion periods during NW was higher, whereas weak inversion periods were more frequent during MRP (see top strip in Fig. 3). As a result, the combined average of strong and weak inversion periods for NW showed differences in characteristics between daytime and nighttime and that for MRP showed similar characteristics during daytime and nighttime (Fig. S7). From this analysis, we conclude that the air masses, in particular their origin and direction, have no influence on aerosol properties in Delhi during late winter and that they are instead dependent on the local meteorological conditions.

Since the megacity is a dominant source of pollution, the different air masses would cause enhanced aerosol concentration only if they originate from another distant and major pollution source. The stubble burning spots in the neighbouring states of Punjab and Haryana during the crop burning season, predominantly during Oct and Nov (Kulkarni et al., 2020) are an example for such a pollution source. Fire spot analysis showed that such a major pollution event was absent during the campaign (see Section2.2) and hence, any air mass originating from outside the city, irrespective of their different locations around the city would have caused dilution effects. This would have contributed to the lower aerosol concentration observed under the more ventilated weak inversion periods (Fig.

S8b and S8d), in contrast to the strong inversion periods (Fig. S8a and S8c) when mixing would have been limited under the shallow PBL.

Additional air mass back trajectory analysis was done using H_{BL} values from WRF as the top of HYSPLIT model (Text S2). The analysis showed that the air mass path was shorter and that they overlapped during most of the time, except when there was a south-east branch during daytime and nighttime of weak inversion periods (Figure S9e, S9f, S9g and S9h). The south-east branch, however, showed no effect on the aerosol properties, because the strong inversion-daytime air masses, which lack this branch of air mass, showed comparable aerosol number and hygroscopicity distribution to that during the weak inversion periods (Fig. S9a and S9b). This shows that, irrespective of the origin and direction of air masses, higher H_{BL} and faster winds facilitate mixing, resulting in similar aerosol properties under such meteorological conditions and hence, the air masses do not have any strong influence on the locally emitted aerosols within Delhi. The above observations lead to the conclusion that the diurnal evolution of H_{BL} is the most important meteorological parameter that locally influences aerosol properties in Delhi, in the absence of any secondary and major source of pollution around the city.

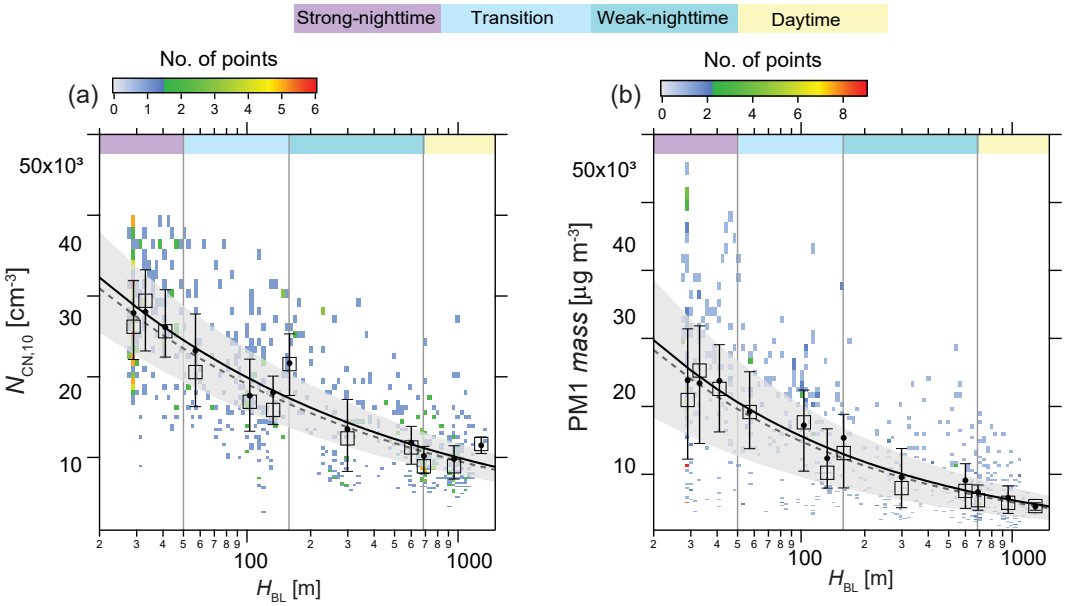

Figure 7. Correlation of H_{BL} with (a): $N_{\mathrm{CN},10}$, (b): PM1. The squares and error bars show the three quartiles of observations in each bin of H_{BL}. The dots indicate average of aerosol properties in each bin. The lines show the fit of correlation to average (solid black line) and median (grey dashed line). The fit to the quartiles are shown as grey shading. There are 733 data points in (a) and 718 data points in (b) and the background shows the pixels coloured by the number of data points.

	$N_{\mathrm{CN,10}}$			PM1		
Fit to	$C_{\max}$	p	R^2	$C_{\max}$	p	R^2
Average	79287	0.4	0.94	493	0.3	0.96
1st quartile	62531	0.4	0.85	303	0.3	0.88
2nd quartile	75981	0.4	0.88	469	0.3	0.92
3rd quartile	93211	0.4	0.95	640	0.3	0.97

Table 2: The parameters and goodness of fit of the correlation between $N_{\mathrm{CN,10}}$ vs. H_{BL} and PM1 vs. H_{BL} in Fig. 7

With the exception of the CCN efficiency (Fig. 3e), all aerosol and CCN properties exhibited a strong dependence on local meteorological parameters, predominantly the H_{BL}. A strong correlation was observed between H_{BL} and the binned averages of aerosol number concentration, PM1 mass concentration (Table 2), and CCN number concentration (N_{CCN}) for three different S levels (Table 3). The bins in each class (top strip of Figure 7 and 8) were selected based on the three most frequently occurring H_{BL} in each class. The width of each bin was determined based on the similarity in trend of the nearest observations. A simple power-law fit provides an effective parameterization for the correlations of binned average concentrations of all the absolute aerosol and CCN properties with H_{BL} over the entire range of height variations. Moreover, the binned 1st and 3rd quartiles of $N_{\mathrm{CN,10}}$ and PM1 mass showed similar variation as the respective median (Fig. 7). Analogously, N_{CCN} at different S levels showed a simple power-law relationship with H_{BL} (Fig. 8). These observations suggest that at different levels of aerosol loading the relationship between $N_{\mathrm{CN,10}}$, PM1 mass, and N_{CCN} and H_{BL} remains unaffected.

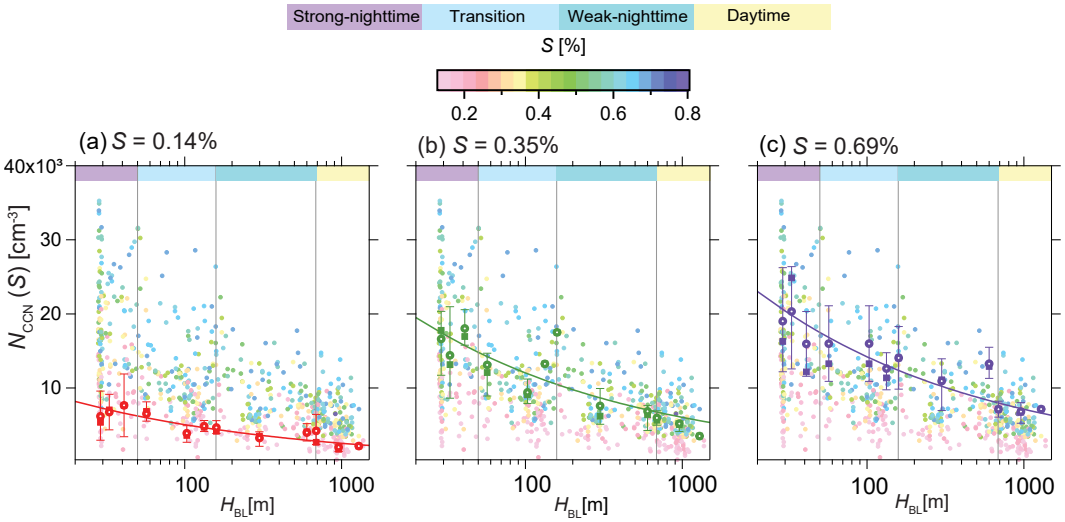

Figure 8. Correlation of H_{BL} with N_{CCN} measured at S (a): 0.14 % (b): 0.35 % and (c): 0.69 %. The squares and error bars show the three quartiles of observations in each bin of H_{BL}. The circles indicate average of CCN concentration in each bin. The solid lines show the fit of correlation to average. There were 65, 68, and 67 data points for $S = 0.14\,\%$, $0.35\,\%$ and $0.69\,\%$ respectively. The background shows all the data points colour-scaled by the S levels.

$N_{\mathrm{CCN}}(S)$	S=0.14 %			S=0.35 %			S=0.69 %		
Fit to	$C_{\max}$	p	R^2	$C_{\max}$	p	R^2	$C_{\max}$	p	R^2
Average	20093	0.3	0.79	47913	0.3	0.91	56559	0.3	0.86

Table 3: The parameters and goodness of fit of the correlation between $N_{\mathrm{CCN}}(S)$ vs. H_{BL} shown in Fig. 8

It is important to note that the effective relationship observed here for use as a possible parameterization is representative of the particular season, local aerosol emissions, and specific meteorological conditions pertaining to this part of the globe. Additional and comprehensive similar measurements over larger spatial areas representing diverse environmental conditions and covering multiple seasons as long-term measurements are important to further validate and prove the relevance of such a parameterization to be effectively used in regional climate models. Nevertheless, the concentration (C) of PM1 mass ($\mu\mathrm{g\,m^{-3}}$), and aerosol and CCN number ($\mathrm{cm^{-3}}$) decreases to the power of H_{BL} (m), and can be represented by Equation 1. The resulting fit parameters are summarized in Tables 2 and 3.

$$C = C_{\max} * {H_{\mathrm{BL}}}^{-\mathrm{p}} \tag{1}$$

The parameterization obtained from the correlation fits physically relates to the changes in aerosol concentration resulting from fluctuations in PBL mixing volume. While the mass concentration decreases to the power of 0.4, the number concentration decreases to the power of 0.3 of H_{BL}. It may also be noted that the variations in H_{BL} are tightly coupled with other meteorological parameters (for example T and RH), which in turn can affect underlying processes and mechanisms of secondary aerosol formation.

Summarizing, firstly, the analysis of average aerosol properties during the daytime and nighttime under different inversion conditions for a given air mass (Fig. S8) indicates that aerosol properties show considerable difference between daytime and nighttime under the strong inversion periods, irrespective of the air mass origin and path. Secondly, the correlation of absolute aerosol and CCN properties with H_{BL} (Fig. 7 and 8) indicates that the difference in the daytime and nighttime aerosol and CCN loading is more pronounced during the strong inversion periods compared to the weak inversion periods. The strong inversion periods are characterized by low H_{BL}, low wind speeds and high RH. Therefore, to better understand the role of H_{BL} and other meteorological parameters on aerosol properties, processing, and potential interaction with water vapour, Figure 9 shows various aerosol properties retrieved from measurements during the two distinct inversion periods separated by daytime and nighttime.

A significant difference in aerosol size and hygroscopicity distribution, and chemical composition was observed between the daytime and nighttime during strong inversion periods (Fig. 9a and 9c). During weak inversion periods, this difference between the daytime and nighttime aerosol properties was either weak or minimal (Fig. 9b and 9d). It should be noted that except strong inversion-nighttime, all other periods showed qualitatively and quantitatively similar characteristics in the average aerosol number size and hygroscopicity distribution. The relatively low κ observed under strong inversion-nighttime (Fig. 9a; Table S4) is attributable to less ventilation within the H_{BL} owing to the following mechanism. The lower ventilation inhibits the aging of freshly emitted aerosols by preventing the mixing with gaseous pollutants within the city and aged and background aerosols from surrounding regions (Pöschl, 2005; Riemer et al., 2019). This is in contrast to situations reported in Gunthe et al. (2011); Rose et al. (2010), where such a mixing is known to enhance the internal mixing with inorganic components, which may lead to higher κ values.

Under the cold and humid conditions persisting during the strong inversion-nighttime, feedback to total aerosol load by pollutants emitted due to increased biofuel use for domestic heating during winter (Dec to Jan) was reported by Hakkim et al. (2019). The aerosol

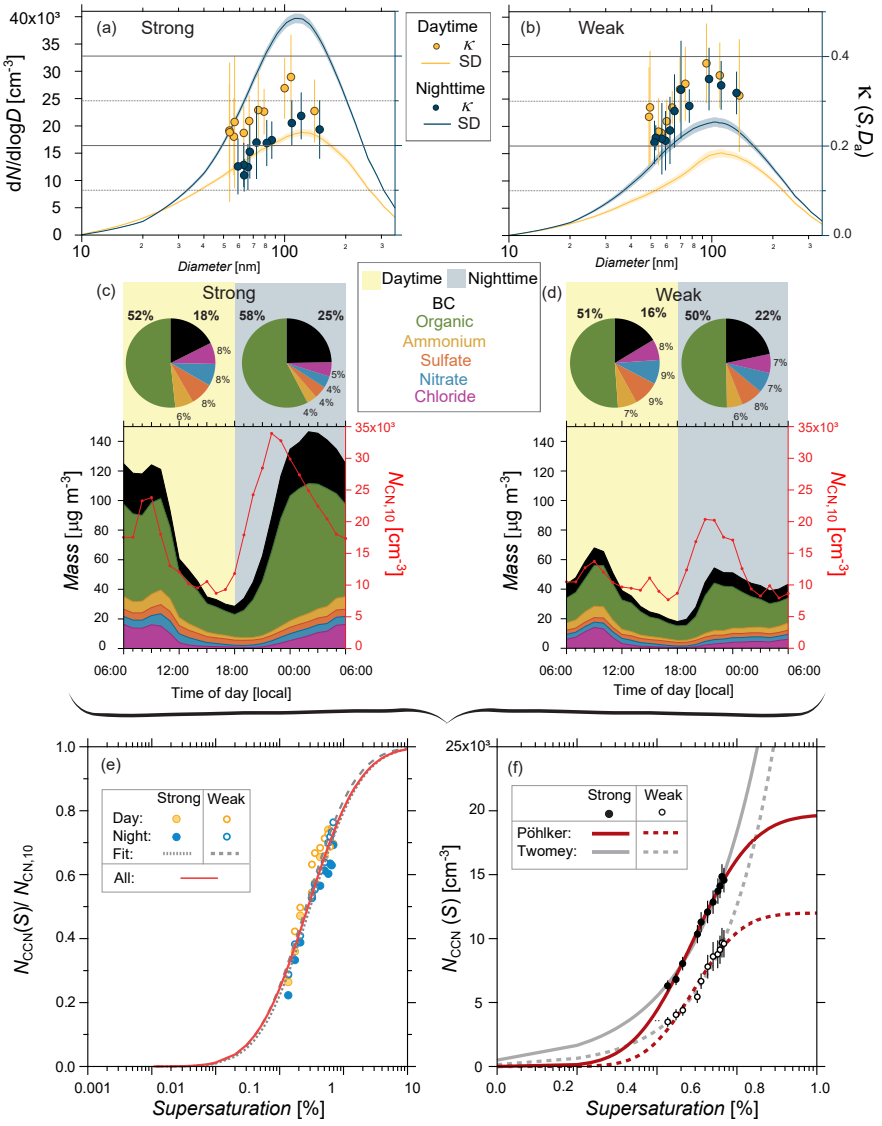

Figure 9. Diurnal average particle number size (left axis) and κ (right axis) distribution during (a): strong inversion periods and (b): weak inversion periods. The error bars are one standard deviation. (c) and (d): The top panel shows the diurnal average PM1 mass fractions; the bottom panel shows the diurnal average cycle of PM1 mass (left axis) and $N_{\mathrm{CN,10}}$ (right axis) under (c): strong inversion and (d): weak inversion periods. (e): Single error-function (erf) fit: $y = 0.5 + 0.5$*erf(ln(S/0.28)/2.09) (Pöhlker et al., 2016) on diurnal average data of strong and weak inversion periods. (f): CCN spectra reproduced using the single erf fit in (e) and measured real-time $N_{\mathrm{CN,10}}$ during strong and weak inversion periods; and the corresponding fits using modified Pöhlker et al. (2016) erf fit (Eq. 3) and Twomey (1959) fit. The parameters of the modified erf fit of CCN spectra are, strong inversions: $A = 19700\,\mathrm{cm}^{-3}$; $S_{\mathrm{o}} = 0.28\,\%$; $w_{\mathrm{o}} = 1.93$, and weak inversions: $A = 12000\,\mathrm{cm}^{-3}$; $S_{\mathrm{o}} = 0.29\,\%$; $w_{\mathrm{o}} = 1.54$.

load is expected to be consistently high if cold weather induced BB burning emission feedback is to take place particularly during low H_{BL} conditions. In contrast, we observed pronounced variation of $N_{\mathrm{CN,10}}$ corresponding to the traffic peak hours during nighttime ($N_{\mathrm{CN,10}}$ in Fig. 9c right panel with grey background) indicating that there was no prominent feedback

from biofuel use to aerosol burden. Instead, variations in H_{BL} alone appeared to be the dominating factor for increased aerosol mass burden. This variation, although quantitatively unsubstantial, was also observed under weak inversion periods ($N_{\mathrm{CN},10}$ in Fig. 9d, right panel with grey background).

The ratios of BC mass to PM1 during nighttime under both strong and weak inversion periods (right panel pie chart over grey background in Fig. 9c and 9d; also see Figure S10) are comparable. A major fraction of BC mass is associated with fossil fuel combustion and this emission scenario remains unchanged during strong as well as weak inversion periods (Figure S11 and S12). However, despite emission sources remaining similar, the quantitative behaviour of the diurnal variation of PM1 mass is different between the strong and weak inversion periods as shown in Fig. 9c and 9d. The PM1 mass concentrations exhibited a pronounced diurnal variation during the strong inversion periods. In contrast, the well-ventilated weak inversion periods showed reduced PM1 mass concentrations of all species leading to weaker diurnal variation. This shows that local meteorological conditions could play an important role in determining the accumulation of PM1 mass within the boundary layer. A lower inorganic mass fraction was observed during strong inversion-nighttime (average f_{inorg}= 17 % in Fig. 9c right panel; see also Fig. S10a) compared to weak inversion-nighttime (average f_{inorg}= 28 % in Fig. 9d right panel; see also Fig. S10b). This indicates that the low H_{BL} during the strong inversion-nighttime, in the absence of any strong winds (Fig. 6a) could have restricted the mixing of polluted air with gaseous emissions, and aged aerosol influx from the nearby and sub-urban region (e.g., the less polluted state of Haryana during late winter (Lalchandani et al., 2021)), which otherwise would have resulted in a higher inorganic mass fraction (Gunthe et al., 2011). On the other hand, during the weak inversion-nighttime H_{BL} is higher, and the winds are relatively faster (Fig. 6a), which could facilitate better mixing of freshly emitted aerosols with gaseous pollutants within the city (Pöschl, 2005), and aged aerosol influx from nearby regions to produce more internally mixed aerosols (Riemer et al., 2019) leading to higher f_{inorg}.

The above observations are also supported by the 13 % lower average MAF across all S levels during strong inversion-nighttime than that during weak inversion-nighttime (see bottom panel in Table S4 and S5). This indicates that the aerosols consist of enhanced portions of externally mixed weakly-CCN active particles under low H_{BL}. Moreover, during daytime, there was only a 3 % difference in average MAF across all S levels under strong and weak inversion conditions. Complementing the above observations, the average MAF across all S levels during strong inversion periods was up to 18 % lower during nighttime than daytime, whereas during weak inversion periods, nighttime showed 9 % lower values than daytime. Hence, we conclude that the shallow nocturnal PBL and smaller mixing volume during strong inversion periods were limiting the internal mixing of fresh city emissions with aged and background aerosols and other gaseous pollutants due to the stagnant conditions caused by lower wind speeds. Hence, we hypothesize that the freshly emitted aerosols possibly undergo rapid chemical transformation and aging under the well mixed layer existing throughout the weak inversion periods, whereas the confined boundary layer during the nighttime of strong inversion may inhibit such a transformation and aging due to limited mixing with gaseous and particulate ingredients for multiphase processes. Thus, H_{BL} appears to be the primary factor influencing aerosol accumulation and chemical processing, followed by emissions.

The influence of local meteorology on aerosol properties in Delhi is in contrast with observations from other megacities, for example Beijing, mainly due to the confined geography of Delhi and the variations in H_{BL} driven by radiative cooling. Studies have shown that aerosol formation and processing over megacities in China are also related to H_{BL}, however, the aerosol properties are not independent of the air mass origin and contributions from regional pollution (Garland et al., 2009; Rose et al., 2011; Zheng et al., 2015). In these cities, a positive feedback to aerosol pollution through aerosol-radiation interaction has also been observed (J. Wang et al., 2014; J. Wu et al., 2019; Tie et al., 2017; Y. Wang et al., 2020), which appeared to be negligible during the late winter in Delhi. Moreover, the mechanism of PBL lowering in Delhi during late winter was predominantly radiative

thermal inversion, unlike the megacities in China where synoptic meteorological processes like frontal inversion or temperature advection play a major role in modulating the H_{BL} (T. Su et al., 2020; Yu et al., 2020; Zheng et al., 2015).

The CCN efficiencies remained consistent throughout the campaign and the average diurnal CCN efficiencies during both strong and weak inversion periods could be fitted well to a single error function (erf) curve as described by Pöhlker et al. (2016) (Equation 2) (Fig. 9e), which has been applied to measurements at the ATTO site (Andreae et al., 2015).

$$N_{\mathrm{CCN}}(S)/N_{\mathrm{CN,10}} = 0.5 + 0.5 * \mathrm{erf}\left(\frac{\ln(\frac{S}{0.28})}{2.09}\right) \tag{2}$$

This implies that CCN efficiencies are not affected by the change in aerosol accumulation and processing under the low H_{BL}. This is because the aerosol size distribution during the strong inversion-nighttime had a pronounced accumulation mode (geometric mean diameter ∼132 nm), and the abundance of larger particles compensated for the effect of reduced hygroscopicity, yielding similar CCN efficiency spectra. This suggests the importance of aerosol particle number and size for effective CCN activation, consistent with previous studies (Dusek et al., 2006; Gunthe et al., 2009, 2011). The high CCN efficiency achieved at the highest measured $S = 0.69\,\%$ during both strong and weak inversion periods (70 % and 74 % ,respectively) also verifies the high activated fractions estimated by Arub et al. (2020).

The combined CCN efficiency spectrum fit (Fig. 9e) is used with the real-time measured $N_{\mathrm{CN,10}}$ during strong and weak inversion periods to reproduce the corresponding averaged CCN spectra (black dots and circles in Fig. 9f), which shows that the sensitivity of N_{CCN} to H_{BL} is captured well using the combined CCN efficiency parameterization. For the reproduced CCN spectra, a modified erf fit (Equation 3)

$$N_{\mathrm{CCN}}(S) = A/2 + A/2 * \mathrm{erf}\left(\frac{\ln(\frac{S}{S_{\mathrm{o}}})}{w_{\mathrm{o}}}\right) \tag{3}$$

based on Pöhlker et al. (2016) (red lines in Fig. 9f) caused the CCN number concentration to converge against the respective $N_{\mathrm{CN,10}}$ at high S levels during strong and weak inversion periods as shown in Fig. 9f (strong inversion periods -$N_{\mathrm{CN,10}}$ = 20,000 cm^3 and weak inversion periods -$N_{\mathrm{CN,10}}$ = 12,300 cm^3). This good agreement indicates that at high S levels all internally mixed particles activate, unlike the unrealistic increase in CCN number concentration exceeding the total available aerosol number concentration at higher S levels that would result from the traditional Twomey fit (Twomey, 1959) (grey lines in Fig. 9f). Therefore, the modified CCN spectra introduced here give a much better physical representation of CCN number concentrations as a function of S levels than the traditional Twomey power-law fit. This effectively shows that the combined CCN efficiency spectra are sufficient for modelling CCN activity using total aerosol load under varying meteorological conditions. The fit parameters of the modified CCN spectra under strong and weak inversion periods are summarized in the caption of Fig. 9. This parametrization, which is easily applicable to estimate CCN number concentrations, is recommended for further use in modeling studies and requires validation using future long-term measurements under diverse environmental conditions and distinct seasons.

5 Summary

We conducted a comprehensive investigation of aerosol and CCN properties in Delhi, combining measurements, remote sensing data, and model simulations. The study showed that H_{BL} coupled with other meteorological variables plays a key role in modulating extensive and intensive aerosol properties. While aerosol properties such as hygroscopicity and mixing state were associated with the changes in H_{BL}, the aerosol number, CCN number and

PM1 mass concentrations were particularly well explained by a simple function of H_{BL}. We observed two distinct meteorological conditions characterized by high and low solar radiation, resulting in strong and weak radiative thermal inversions and subsequent strong and weak diurnal variations of the modelled H_{BL}. The pronounced diurnal variation of aerosol and CCN concentration, hygroscopicity and mixing state during the strong inversion periods, despite exhibiting similar emissions to weak inversion periods, supports the hypothesis that H_{BL} is the major factor affecting aerosol build up in the local atmosphere of Delhi. We suggest that the distinct meteorological processes in the geographically confined and poorly ventilated Delhi air basin may further enhance the significance of local meteorology in modulating aerosol accumulation and subsequently other aerosol multiphase processes. We present a set of parameterizations, which best explain the behaviour and dependence of extensive aerosol properties, encompassing the correlation of PM1 mass, aerosol and CCN number concentrations to H_{BL}, and CCN activity for this campaign.

The air mass back trajectory analysis revealed weak influence of the air mass origin and path on the aerosol properties, since the air masses originated from and traversed over regions that were relatively less polluted than the local surroundings. Only during the crop residue burning season (Oct and Nov), another major pollution source outside the megacity is present. Without this source during the late winter, the surrounding regions do not significantly affect the aerosol properties in Delhi. The local wind direction also had no effect on aerosols, implying that the measured aerosol and CCN properties are representative of the metropolitan area.

The H_{BL} correlated well with the aerosol and CCN number concentrations and the PM1 mass concentrations. These characteristic aerosol properties can be described as a simple power law function of H_{BL}. The aerosol hygroscopicity, although less affected by H_{BL} was lower during the low H_{BL} experienced during the nighttime of strong inversion periods. During the same period, the maximum activated fractions were also lower, indicating enhanced external mixing compared to the other periods. This change in hygroscopicity, mixing state, and the lower inorganic mass fraction in PM1 during strong inversion-nighttime under unchanged emissions, can be explained by the hypothesis that mixing of aerosols with gaseous pollutants within the city, and aged aerosol influx from outside the megacity was inhibited by low wind speeds under the shallow nocturnal PBL. Therefore, such a major influence of PBL height on aerosol accumulation and processing appears to be specific to Delhi, making it distinct from comparably polluted megacities in China.

Regardless of the change in aerosol number and composition caused by the strong variations in H_{BL}, the CCN efficiencies were unaffected and remained consistent for the whole measurement period. Hence, a single parameterization could model the CCN efficiency spectrum, which captured the variability in CCN concentration under varying meteorological conditions. The CCN efficiency spectrum is well represented by the error function fit (Equation 2; Pöhlker et al. (2016)) and the CCN spectra are well represented by the modified Pöhlker et al. (2016) error function fit (Equation 3).

Our study shows that the CCN number variability, which relates to the interaction of aerosols with water vapour in the polluted atmosphere of Delhi primarily depends on the local meteorologically coupled processes during late winter. However, the CCN efficiency remains unaffected due to the ubiquitous nature of accumulation mode particles in the megacity's PBL. These particles in the accumulation mode not only can adversely affect public health (Andersen et al., 2008; Fonceca et al., 2018), but can also deteriorate atmospheric visibility by efficient light scattering and extinction (Waggoner et al., 1981; Jacobson, 2005). The PBL in Delhi contains abundant efficient CCN, which can form fog and haze under the high humidity conditions prevalent during late winter. Moreover, the elevated CCN particles can enter clouds and contribute to cloud microphysical effects (Stocker et al., 2013), implying changes to the aerosol-cloud interaction induced radiative forcing in Delhi. Our findings are expected to improve the representation of aerosols and CCN activity particularly over the Indian region, where accurate measurements are sparse. This will help to formulate control measures for improving regional air quality and mitigating public health impacts.

It is important to note that the interactions between meteorology and aerosol properties presented here are specific to the location and season of the year. Thus, more measurements under varying environmental conditions for longer duration are urgently required for validation and further improvement of the proposed parameterizations. Such measurements during the different seasons of the Indian sub-continent with special attention to the IGP region are recommended. Nevertheless, our measurements highlight the important relation between meteorology and aerosol properties and the effects it may have on fog and haze formation over Delhi. Further, the detailed information and parameterization presented here could enable efficient description of the role of meteorology induced aerosol processes and implications for fog and haze formation over Delhi during this season in aerosol property and process models.

Glossary

A Aerosol number concentration derived from erf fit of CCN spectra, cm^{-3}
$\boldsymbol{D_a}$ Midpoint activation diameter derived from CDF of measured activation curves, nm
$\boldsymbol{D_m}$ Modal diameter of the aerosol number size distribution, nm
$\boldsymbol{f_{org}}$ Organic mass fraction in PM1
$\boldsymbol{f_{inorg}}$ Inorganic mass fraction in PM1
$\boldsymbol{H_{BL}}$ Modelled height of planetary boundary layer, m
$\boldsymbol{M_{BC,e}}$ Mass of equivalent black carbon, $\mu g\,m^{-3}$
$\boldsymbol{MAF(S)}$ Maximum activated fraction at given S level
$\boldsymbol{N_{CCN}(S)}$ CCN number concentration at given S level, cm^{-3}
$\boldsymbol{N_{CN,10}}$ Aerosol number concentration (10 to 370 nm) in the measured sample, cm^{-3}
$\boldsymbol{RH}$ Relative humidity, %
$\boldsymbol{S}$ Effective supersaturation measured inside the CCNC column, %
$\boldsymbol{T}$ Temperature, °C
$\kappa(\boldsymbol{S},\boldsymbol{D_a})$ Effective particle hygroscopicity corresponding to size D_a measured at S

Acronyms

ACSM Aerosol chemical speciation monitor
ATTO Amazon tall tower observatory
BB Biomass burning
BC Black carbon
BT Back trajectory
CCN Cloud condensation nuclei
CCNC Cloud condensation nuclei counter
CDF Cumulative distribution function
DMA Differential mobility analyzer
EC Electrostatic classifier
ECMWF European Centre for Medium-Range Weather Forecasts
ERA5 ECMWF Reanalysis 5th Generation
HYSPLIT The Hybrid Single Particle Legrangian Integrated Trajectory model
IGP Indo-Gangetic Plain
MDF Minimum average flip distance
MRP Mixed regional pollution
NR-PM1 Non refractory particulate matter of size less than 1 μm
NW North-west
PBL Planetary boundary layer
PM1 Particulate matter of size less than 1 μm

SE South-east
UCPC Ultrafine condensation particle counter
WRF The Weather Research and Forecasting model

Acknowledgments
SSG gratefully acknowledges funding from Ministry of Earth Sciences (MoES; sanction number MoES/16/20/12-RDEAS dated 31.Mar.2014), Government of India, for the purchase of the Cloud Condensation Nuclei Counter (CCNC). This work was supported by partial funding from the Ministry of Earth Sciences (MoES; sanction number MoES/16/04/2017-APHH (PROMOTE)), Government of India. This work was also partially supported by the UK Natural Environment Research Council and the Newton Fund through the PROMOTE project of the APHH-Delhi programme, grant ref. NE/P016480/1 and NE/P016472/1. All the authors are grateful to the APHH-PROMOTE team for providing logistic and experimental support during the campaign. We thank Alfatech Services, New Delhi, for their generous technical support during the campaign. We thank the Max Planck super computing facility (COBRA) for the support in WRF modelling. SSR was the recipient of a scholarship from the Indo-German Centre for Sustainability through the German Academic Exchange Service under the initiative 'A New Passage to India' funded through the Federal Ministry for Education and Research in 2019 and 2020. SSR, MLP and SSG acknowledge this support for conducting in-person and virtual discussions. SSR acknowledges the team at Max Planck Institute for Chemistry for facilitating the research stay and discussions. SSR also acknowledges the Ministry of Human Resources Development, Government of India for a fellowship.

Open Research
The data associated with key results have been deposited in associated data files in an open research repository. The time series of corrected data from size-resolved CCN experiments (named "CCN.dat"); time series of inverted particle number size distribution (named "SD.dat"); and campaign average of CCN properties (named "AvgCCN.dat") are available in NASA Ames format under https://dx.doi.org/10.17617/3.5y (Raj et al., 2021).

Author Contribution
SSG conceived the idea and designed the research. SSG, GM, and HC conceptualized and planned the field measurement campaign. SSR led the logistic planning and execution of the field campaign. SSR, AS, U. Panda, ED, and SS, carried out robust calibrations and extensive field measurements and collected CCN and ACSM data. MLP and SSR led the CCN data analysis with help from TK. SSR led the size data inversion with help from TK and MLP. SSR led the back trajectory data analysis with help from DW, J-DF, and CP. SSR led the fire spot analysis with help from DW and OK. U. Panda and JA carried out the ACSM data analysis. SSR, MLP, and SSG led the CCN data interpretation with inputs from OK and RR. SSG, RR, U. Panda and SSR led the ACSM data interpretation with inputs from JA, GM, and HC. VKS and RPS provided meteorological data and SSR led the interpretation. SSR wrote the first draft of the manuscript under the mentorship of SSG, with critical edits and inputs form MLP, and comments from STM, U. Pöschl, and MOA. All the co-authors discussed the results and commented on the manuscript.

References

Andersen, Z. J., Wahlin, P., Raaschou-Nielsen, O., Ketzel, M., Scheike, T., & Loft, S. (2008). Size distribution and total number concentration of ultrafine and accumulation mode particles and hospital admissions in children and the elderly in Copenhagen, Denmark. *Occupational and Environmental Medicine*, *65*(7), 458–466. doi: 10.1136/oem.2007.033290

Andreae, M. O., Acevedo, O. C., Araùjo, A., Artaxo, P., Barbosa, C. G. G., Barbosa, H. M. J., Brito, J., Carbone, S., Chi, X., Cintra, B. B. L., da Silva,

N. F., Dias, N. L., Dias-Júnior, C. Q., Ditas, F., Ditz, R., Godoi, A. F. L., Godoi, R. H. M., Heimann, M., Hoffmann, T., Kesselmeier, J., Könemann, T., Krüger, M. L., Lavric, J. V., Manzi, A. O., Lopes, A. P., Martins, D. L., Mikhailov, E. F., Moran-Zuloaga, D., Nelson, B. W., Nölscher, A. C., Santos Nogueira, D., Piedade, M. T. F., Pöhlker, C., Pöschl, U., Quesada, C. A., Rizzo, L. V., Ro, C.-U., Ruckteschler, N., Sá, L. D. A., de Oliveira Sá, M., Sales, C. B., dos Santos, R. M. N., Saturno, J., Schöngart, J., Sörgel, M., de Souza, C. M., de Souza, R. A. F., Su, H., Targhetta, N., Tóta, J., Trebs, I., Trumbore, S., van Eijck, A., Walter, D., Wang, Z., Weber, B., Williams, J., Winderlich, J., Wittmann, F., Wolff, S., & Yáñez Serrano, A. M. (2015). The Amazon Tall Tower Observatory (ATTO): overview of pilot measurements on ecosystem ecology, meteorology, trace gases, and aerosols. *Atmospheric Chemistry and Physics*, *15*(18), 10723–10776. doi: 10.5194/acp-15-10723-2015

Arub, Z., Bhandari, S., Gani, S., Apte, J. S., Hildebrandt Ruiz, L., & Habib, G. (2020). Air mass physiochemical characteristics over New Delhi: impacts on aerosol hygroscopicity and cloud condensation nuclei (CCN) formation. *Atmospheric Chemistry and Physics*, *20*(11), 6953–6971. doi: 10.5194/acp-20-6953-2020

Arun, S. H., Sharma, S. K., Chaurasia, S., Vaishnav, R., & Kumar, R. (2018). Fog/low clouds detection over the Delhi Earth Station using the Ceilometer and the INSAT-3D/3DR satellite data. *International Journal of Remote Sensing*, *39*(12), 4130–4144. doi: 10.1080/01431161.2018.1454624

Asa-Awuku, A., Sorooshian, A., Flagan, R. C., Seinfeld, J. H., & Nenes, A. (2015). CCN properties of organic aerosol collected below and within marine stratocumulus clouds near Monterey, California. *Atmosphere*, *6*(11), 1590–1607. doi: 10.3390/atmos6111590

Atwood, S. A., Reid, J. S., Kreidenweis, S. M., Blake, D. R., Jonsson, H. H., Lagrosas, N. D., Xian, P., Reid, E. A., Sessions, W. R., & Simpas, J. B. (2017). Size-resolved aerosol and cloud condensation nuclei (CCN) properties in the remote marine South China Sea–Part 1: Observations and source classification. *Atmospheric Chemistry and Physics*, *17*(2), 1105–1123. doi: 10.5194/acp-17-1105-2017

Bhandari, S., Gani, S., Patel, K., Wang, D. S., Soni, P., Arub, Z., Habib, G., Apte, J. S., & Hildebrandt Ruiz, L. (2020). Sources and atmospheric dynamics of organic aerosol in New Delhi, India: insights from receptor modelling. *Atmospheric Chemistry and Physics*, *20*(2), 735–752. doi: 10.5194/acp-20-735-2020

Bhattu, D., Tripathi, S. N., & Chakraborty, A. (2016). Deriving aerosol hygroscopic mixing state from size-resolved CCN activity and HR-ToF-AMS measurements. *Atmospheric Environment*, *142*, 57–70. doi: 10.1016/j.atmosenv.2016.07.032

Boucher, O., Randall, D., Artaxo, P., Bretherton, C., Feingold, G., Forster, P., Kerminen, V.-M., Kondo, Y., Liao, H., Lohmann, U., Rasch, P., Satheesh, S., Sherwood, S., Stevens, B., & Zhang, X. (2013). Cloud and Aerosols. In: *Climate Change 2013: The Physical Science Basis. Contribution of Working Group I to the Fifth Assessment Report of the Intergovernmental Panel on Climate Change* [Stocker, T.F., D. Qin, G.-K. Plattner, M. Tignor, S.K. Allen, J. Boschung, A. Nauels, Y. Xia, V. Bex and P.M. Midgley (eds.)]. *Cambridge University Press, Cambridge, United Kingdom and New York, NY, USA*.

Che, H. C., Zhang, X. Y., Zhang, L., Wang, Y. Q., Zhang, Y. M., Shen, X. J., Ma, Q. L., Sun, J. Y., & Zhong, J. T. (2017). Prediction of size-resolved number concentration of cloud condensation nuclei and long-term measurements of their activation characteristics. *Scientific Reports*, *7*(1), 1–12. doi: 10.1038/s41598-017-05998-3

Cheng, Y., Zheng, G., Wei, C., Mu, Q., Zheng, B., Wang, Z., Gao, M., Zhang, Q., He, K., Carmichael, G., Pöschl, U., & Su, H. (2016). Reactive nitrogen chemistry in aerosol water as a source of sulfate during haze events in China. *Science Advances*, *2*(12), e1601530. doi: 10.1126/sciadv.1601530

Dhangar, N. G., Lal, D. M., Ghude, S. D., Kulkarni, R., Parde, A. N., Pithani, P., Niranjan, K., Prasad, D. S. V. V. D., Jena, C., Sajjan, V. S., Prabhakaran, T., Karipot, A. K., K, J. R., Singh, S., & M, R. (2021). On the Conditions for Onset and Development of Fog Over New Delhi: An Observational Study from the WiFEX. *Pure and Applied Geophysics*, 1–20. doi: 10.1007/s00024-021-02800-4

Dumka, U. C., Tiwari, S., Kaskaoutis, D. G., Soni, V. K., Safai, P. D., & Attri, S. D. (2019). Aerosol and pollutant characteristics in Delhi during a winter research campaign. *Environmental Science and Pollution Research*, *26*(4), 3771–3794. doi: 10.1007/s11356-018-3885-y

Dusek, U., Frank, G. P., Hildebrandt, L., Curtius, J., Schneider, J., Walter, S., Chand, D., Drewnick, F., Hings, S., Jung, D., Borrmann, S., & Andreae, M. O. (2006). Size matters more than chemistry for cloud-nucleating ability of aerosol particles. *Science*, *312*(5778), 1375–1378. doi: 10.1126/science.1125261

Fonceca, A. M., Zosky, G. R., Bozanich, E. M., Sutanto, E. N., Kicic, A., McNamara, P. S., Knight, D. A., Sly, P. D., Turner, D. J., & Stick, S. M. (2018). Accumulation mode particles and LPS exposure induce TLR-4 dependent and independent inflammatory responses in the lung. *Respiratory research*, *19*(1), 1–10. doi: doi.org/10.1186/s12931-017-0701-z

Frank, G. P., Dusek, U., & Andreae, M. O. (2006). Technical note: A method for measuring size-resolved ccn in the atmosphere. *Atmospheric Chemistry and Physics Discussions*, *6*, 4879–4895. doi: 10.5194/acpd-6-4879-2006

Gani, S., Bhandari, S., Patel, K., Seraj, S., Soni, P., Arub, Z., Habib, G., Hildebrandt Ruiz, L., & Apte, J. S. (2020). Particle number concentrations and size distribution in a polluted megacity: the Delhi Aerosol Supersite study. *Atmospheric Chemistry and Physics*, *20*(14), 8533–8549. doi: 10.5194/acp-20-8533-2020

Gani, S., Bhandari, S., Seraj, S., Wang, D. S., Patel, K., Soni, P., Arub, Z., Habib, G., Hildebrandt Ruiz, L., & Apte, J. S. (2019). Submicron aerosol composition in the world's most polluted megacity: the Delhi Aerosol Supersite study. *Atmospheric Chemistry and Physics*, *19*(10), 6843–6859. doi: 10.5194/acp-19-6843-2019

Garland, R. M., Schmid, O., Nowak, A., Achtert, P., Wiedensohler, A., Gunthe, S. S., Takegawa, N., Kita, K., Kondo, Y., Hu, M., Shao, M., Zeng, L. M., Zhu, T., Andreae, M. O., & Pöschl, U. (2009). Aerosol optical properties observed during Campaign of Air Quality Research in Beijing 2006 (CAREBeijing-2006): Characteristic differences between the inflow and outflow of Beijing city air. *Journal of Geophysical Research: Atmospheres*, *114*(D2). doi: 10.1029/2008JD010780

Garyfallidis, E., Brett, M., Correia, M. M., Williams, G. B., & Nimmo-Smith, I. (2012). Quickbundles, a method for tractography simplification. *Frontiers in Neuroscience*, *6*, 175. doi: 10.3389/fnins.2012.00175

Gopalakrishnan, S. G., Sharan, M., McNider, R., & Singh, M. P. (1998). Study of radiative and turbulent processes in the stable boundary layer under weak wind conditions. *Journal of the Atmospheric Sciences*, *55*(6), 954–960. doi: 10.1175/1520-0469(1998)055⟨0954:SORATP⟩2.0.CO;2

Gunn, R. (1954). Diffusion Charging of Atmospheric Droplets by Ions, and the Resulting Combination Coefficients. *Journal of Atmospheric Sciences*, *11*(5), 339-347. doi: 10.1175/1520-0469(1954)011⟨0339:DCOADB⟩2.0.CO;2

Gunthe, S. S., King, S. M., Rose, D., Chen, Q., Roldin, P., Farmer, D. K., Jimenez, J. L., Artaxo, P., Andreae, M. O., Martin, S. T., & Pöschl, U. (2009).

Cloud condensation nuclei in pristine tropical rainforest air of Amazonia: size-resolved measurements and modelling of atmospheric aerosol composition and CCN activity. *Atmospheric Chemistry and Physics*, *9*(19), 7551–7575. doi: 10.5194/acp-9-7551-2009

Gunthe, S. S., Liu, P., Panda, U., Raj, S. S., Sharma, A., Darbyshire, E., Reyes-Villegas, E., Allan, J., Chen, Y., Wang, X., Song, S., Pöhlker, M. L., Shi, L., Wang, Y., Kommula, S. M., Liu, T., Ravikrishna, R., McFiggans, G., Mickley, L. J., Martin, S. T., Pöschl, U., Andreae, M. O., & Coe, H. (2021). Enhanced aerosol particle growth sustained by high continental chlorine emission in India. *Nature Geoscience*, *14*(2), 77–84. doi: 10.1038/s41561-020-00677-x

Gunthe, S. S., Rose, D., Su, H., Garland, R. M., Achtert, P., Nowak, A., Wiedensohler, A., Kuwata, M., Takegawa, N., Kondo, Y., Hu, M., Shao, M., Zhu, T., Andreae, M. O., & Pöschl, U. (2011). Cloud condensation nuclei (CCN) from fresh and aged air pollution in the megacity region of Beijing. *Atmospheric Chemistry and Physics*, *11*(21), 11023–11039. doi: 10.5194/acp-11-11023-2011

Guttikunda, S. K., & Calori, G. (2013). A GIS based emissions inventory at 1 km× 1 km spatial resolution for air pollution analysis in Delhi, India. *Atmospheric Environment*, *67*, 101–111. doi: 10.1016/j.atmosenv.2012.10.040

Guttikunda, S. K., & Gurjar, B. R. (2012). Role of meteorology in seasonality of air pollution in megacity Delhi, India. *Environmental Monitoring and Assessment*, *184*(5), 3199–3211. doi: 10.1007/s10661-011-2182-8

Hakkim, H., Sinha, V., Chandra, B. P., Kumar, A., Mishra, A., Sinha, B., Sharma, G., Pawar, H., Sohpaul, B., Ghude, S. D., Pithani, P., Kulkarni, R., Jenamani, R. K., & Rajeevan, M. (2019). Volatile organic compound measurements point to fog-induced biomass burning feedback to air quality in the megacity of Delhi. *Science of The Total Environment*, *689*, 295–304. doi: 10.1016/j.scitotenv.2019.06.438

Henning, S., Dieckmann, K., Ignatius, K., Schäfer, M., Zedler, P., Harris, E., Sinha, B., van Pinxteren, D., Mertes, S., Birmili, W., Merkel, M., Wu, Z., Wiedensohler, A., Wex, H., Herrmann, H., & Stratmann, F. (2014). Influence of cloud processing on CCN activation behaviour in the Thuringian Forest, Germany during HCCT-2010. *Atmospheric Chemistry and Physics*, *14*(15), 7859–7868. doi: 10.5194/acp-14-7859-2014

Iwamoto, Y., Kinouchi, K., Watanabe, K., Yamazaki, N., & Matsuki, A. (2016). Simultaneous measurement of CCN activity and chemical composition of fine-mode aerosols at Noto peninsula, Japan, in autumn 2012. *Aerosol and Air Quality Research*, *16*(9), 2107–2118. doi: 10.4209/aaqr.2015.09.0545

Jacobson, M. Z. (2005). *Fundamentals of Atmospheric Modeling* (2nd ed.). Cambridge University Press. doi: 10.1017/CBO9781139165389

Jacobson, M. Z., Nghiem, S. V., & Sorichetta, A. (2019). Short-Term Impacts of the Megaurbanizations of New Delhi and Los Angeles Between 2000 and 2009. *Journal of Geophysical Research: Atmospheres*, *124*(1), 35–56. doi: 10.1029/2018JD029310

Jain, M., Dawa, D., Mehta, R., Dimri, A., & Pandit, M. (2016). Monitoring land use change and its drivers in Delhi, India using multi-temporal satellite data. *Modelling Earth Systems and Environment*, *2*(1), 19. doi: 10.1007/s40808-016-0075-0

Jaiprakash, A., Singhai, Habib, G., Raman, R. S., & Gupta, T. (2017). Chemical characterization of PM 1.0 aerosol in Delhi and source apportionment using positive matrix factorization. *Environmental Science and Pollution Research*, *24*(1), 445–462. doi: 10.1007/s11356-016-7708-8

Jayachandran, V. N., Babu, S. N. S., Vaishya, A., Gogoi, M. M., Nair, V. S., Satheesh, S. K., & Moorthy, K. K. (2020). Altitude profiles of cloud

condensation nuclei characteristics across the Indo-Gangetic Plain prior to the onset of the Indian summer monsoon. *Atmospheric Chemistry and Physics*, *20*(1), 561–576. doi: 10.5194/acp-20-561-2020

Knutson, E., & Whitby, K. (1975). Aerosol classification by electric mobility: apparatus, theory, and applications. *Journal of Aerosol Science*, *6*(6), 443-451. doi: 10.1016/0021-8502(75)90060-9

Kulkarni, S. H., Ghude, S. D., Jena, C., Karumuri, R. K., Sinha, B., Sinha, V., Kumar, R., Soni, V. K., & Khare, M. (2020). How much does large-scale crop residue burning affect the air quality in delhi? *Environmental Science & Technology*, *54*(8), 4790–4799. doi: 10.1021/acs.est.0c00329

Kumar, N., Soni, K., Garg, N., Agarwal, R., Saha, D., Singh, M., & Singh, G. (2017). SODAR pattern classification and its dependence on meteorological parameters over a semiarid region of India. *International Journal of Remote Sensing*, *38*(11), 3466–3482. doi: 10.1080/01431161.2017.1294774

Lalchandani, V., Kumar, V., Tobler, A., Thamban, N. M., Mishra, S., Slowik, J. G., Bhattu, D., Rai, P., Satish, R., Ganguly, D., Tiwari, S., Rastogi, N., Tiwari, S., Močnik, G., Prévôt, A. S. H., & N, T. S. (2021). Real-time characterization and source apportionment of fine particulate matter in the Delhi megacity area during late winter. *Science of the Total Environment*, *770*, 145324. doi: 10.1016/j.scitotenv.2021.145324

Lelieveld, J., Pozzer, A., Pöschl, U., Fnais, M., Haines, A., & Münzel, T. (2020). Loss of life expectancy from air pollution compared to other risk factors: a worldwide perspective. *Cardiovascular Research*, *116*(11), 1910–1917. doi: 10.1093/cvr/cvaa025

Ma, Y., Li, S., Zheng, J., Khalizov, A., Wang, X., Wang, Z., & Zhou, Y. (2017). Size-resolved measurements of mixing state and cloud-nucleating ability of aerosols in Nanjing, China. *Journal of Geophysical Research: Atmospheres*, *122*(17), 9430–9450. doi: 10.1002/2017JD026583

Mandal, P., Sarkar, R., Mandal, A., & Saud, T. (2014). Seasonal variation and sources of aerosol pollution in Delhi, India. *Environmental Chemistry Letters*, *12*(4), 529–534. doi: 10.1007/s10311-014-0479-x

Murthy, B., Latha, R., Tiwari, A., Rathod, A., Singh, S., & Beig, G. (2020). Impact of mixing layer height on air quality in winter. *Journal of Atmospheric and Solar-Terrestrial Physics*, *197*, 105157. doi: 10.1016/j.jastp.2019.105157

Ng, N. L., Herndon, S. C., Trimborn, A., Canagaratna, M. R., Croteau, P. L., Onasch, T. B., Sueper, D., Worsnop, D. R., Zhang, Q., Sun, Y. L., & Jayne, J. T. (2011). An Aerosol Chemical Speciation Monitor (ACSM) for routine monitoring of the composition and mass concentrations of ambient aerosol. *Aerosol Science and Technology*, *45*(7), 780–794. doi: 10.1080/02786826.2011.560211

Ojha, N., Sharma, A., Kumar, M., Girach, I., Ansari, T. U., Sharma, S. K., Singh, N., Pozzer, A., & Gunthe, S. S. (2020). On the widespread enhancement in fine particulate matter across the Indo-Gangetic Plain towards winter. *Scientific Reports*, *10*(1), 1–9. doi: 10.1038/s41598-020-62710-8

Paramonov, M., Kerminen, V.-M., Gysel, M., Aalto, P. P., Andreae, M. O., Asmi, E., Baltensperger, U., Bougiatioti, A., Brus, D., Frank, G. P., Good, N., Gunthe, S. S., Hao, L., Irwin, M., Jaatinen, A., Jurányi, Z., King, S. M., Kortelainen, A., Kristensson, A., Lihavainen, H., Kulmala, M., Lohmann, U., Martin, S. T., McFiggans, G., Mihalopoulos, N. A., N., O'Dowd, C. D., Ovadnevaite, J., Petäjä, T., Pöschl, U., Roberts, G. C., Rose, D., Svenningsson, B., Swietlicki, E., Weingartner, E., Whitehead, J., Wiedensohler, A., Wittbom, C., & Sierau, B. (2015). A synthesis of cloud condensation nuclei counter (CCNC) measurements within the EUCAARI network. *Atmospheric Chemistry and Physics*, *15*(21), 12211–12229. doi: 10.5194/acp-15-12211-2015

Pasricha, P. K., Gera, B. S., Shastri, S., Maini, H. K., John, T., Ghosh, A. B., Tiwari, M. K., & Garg, S. C. (2003). Role of the water vapour greenhouse effect in the forecasting of fog occurrence. *Boundary-Layer Meteorology*, *107*(2), 469–482. doi: 10.1023/A:1022128800130

Paul, S., Saxena, K. G., Nagendra, H., & Lele, N. (2021). Tracing land use and land cover change in peri-urban Delhi, India, over 1973–2017 period. *Environmental Monitoring and Assessment*, *193*(2), 1–12. doi: 10.1007/s10661-020-08841-x

Petters, M., & Kreidenweis, S. (2007). A single parameter representation of hygroscopic growth and cloud condensation nucleus activity. *Atmospheric Chemistry and Physics*, *7*(8), 1961–1971. doi: 10.5194/acp-7-1961-2007

Pöhlker, M. L., Ditas, F., Saturno, J., Klimach, T., Hrabě de Angelis, I., Araùjo, A. C., Brito, J., Carbone, S., Cheng, Y., Chi, X., Ditz, R., Gunthe, S. S., Holanda, B. A., Kandler, K., Kesselmeier, J., Könemann, T., Krüger, O. O., Lavrič, J. V., Martin, S. T., Mikhailov, E., Moran-Zuloaga, D., Rizzo, L. V., Rose, D., Su, H., Thalman, R., Walter, D., Wang, J., Wolff, S., Barbosa, H. M. J., Artaxo, P., Andreae, M. O., Pöschl, U., & Pöhlker, C. (2018). Long-term observations of cloud condensation nuclei over the Amazon rain forest–Part 2: Variability and characteristics of biomass burning, long-range transport, and pristine rain forest aerosols. *Atmospheric Chemistry and Physics*, *18*(14), 10289–10331. doi: 10.5194/acp-18-10289-2018

Pöhlker, M. L., Pöhlker, C., Ditas, F., Klimach, T., Hrabe de Angelis, I., Araújo, A., Brito, J., Carbone, S., Cheng, Y., Chi, X., Ditz, R., Gunthe, S. S., Kesselmeier, J., Könemann, T., Lavrič, J. V., Martin, S. T., Mikhailov, E., Moran-Zuloaga, D., Rose, D., Saturno, J., Su, H., Thalman, R., Walter, D., Wang, J., Wolff, S., Barbosa, H. M. J., Artaxo, P., Andreae, M. O., & Pöschl, U. (2016). Long-term observations of cloud condensation nuclei in the Amazon rain forest–Part 1: Aerosol size distribution, hygroscopicity, and new model parametrizations for CCN prediction. *Atmospheric Chemistry and Physics*, *16*(24), 15709–15740. doi: 10.5194/acp-16-15709-2016

Pöschl, U. (2005). Atmospheric aerosols: composition, transformation, climate and health effects. *Angewandte Chemie International Edition*, *44*(46), 7520–7540. doi: 10.1002/anie.200501122

Raatikainen, T., Hyvärinen, A.-P., Hatakka, J., Panwar, T., Hooda, R., Sharma, V., & Lihavainen, H. (2011). Comparison of aerosol properties from the Indian Himalayas and the Indo-Gangetic plains. *Atmospheric Chemistry and Physics Discussions*, *11*(4), 11417–11453. doi: 10.1016/j.atmosenv.2014.02.058

Raj, S. S., Pöhlker, M., Sharma, A., & Gunthe, S. S. (2021). Delhi size-resolved CCN, PBL and SD data in Raj et al. 2021. *Max Planck Society*. doi: 10.17617/3.5y

Reyes-Villegas, E., Panda, U., Darbyshire, E., Cash, J. M., Joshi, R., Langford, B., Di Marco, C. F., Mullinger, N. J., Alam, M. S., Crilley, L. R., Rooney, D. J., Acton, W. J. F., Drysdale, W., Nemitz, E., Flynn, M., Voliotis, A., McFiggans, G., Coe, H., Shivani, Gadi, R., Singh, S., Soni, V., & Allan, J. D. (2021). PM_1 composition and source apportionment at two sites in Delhi, India, across multiple seasons. *Atmospheric Chemistry and Physics*, *21*(15), 11655–11667. doi: 10.5194/acp-21-11655-2021

Riemer, N., Ault, A. P., West, M., Craig, R. L., & Curtis, J. H. (2019). Aerosol mixing state: Measurements, modeling, and impacts. *Reviews of Geophysics*, *57*(2), 187–249. doi: 10.1029/2018RG000615

Roberts, G. C., & Nenes, A. (2005). A continuous-flow streamwise thermal-gradient CCN chamber for atmospheric measurements. *Aerosol Science and Technology*, *39*(3), 206–221. doi: 10.1080/027868290913988

Rose, D., Gunthe, S. S., Mikhailov, E., Frank, G., Dusek, U., Andreae, M. O., & Pöschl, U. (2008). Calibration and measurement uncertainties of a continuous-flow cloud condensation nuclei counter (DMT-CCNC): CCN

activation of ammonium sulfate and sodium chloride aerosol particles in theory and experiment. *Atmospheric Chemistry and Physics*, *8*(5), 1153–1179. doi: 10.5194/acp-8-1153-2008

Rose, D., Gunthe, S. S., Su, H., Garland, R. M., Yang, H., Berghof, M., Cheng, Y. F., Wehner, B., Achtert, P., Nowak, A., Wiedensohler, A., Takegawa, N., Kondo, Y., Hu, M., Zhang, Y., Andreae, M. O., & Pöschl, U. (2011). Cloud condensation nuclei in polluted air and biomass burning smoke near the mega-city Guangzhou, China–Part 2: Size-resolved aerosol chemical composition, diurnal cycles, and externally mixed weakly CCN-active soot particles. *Atmospheric Chemistry and Physics*, *11*(6), 2817–2836. doi: 10.5194/acp-11-2817-2011

Rose, D., Nowak, A., Achtert, P., Wiedensohler, A., Hu, M., Shao, M., Zhang, Y., Andreae, M. O., & Pöschl, U. (2010). Cloud condensation nuclei in polluted air and biomass burning smoke near the mega-city Guangzhou, China–Part 1: Size-resolved measurements and implications for the modelling of aerosol particle hygroscopicity and CCN activity. *Atmospheric Chemistry and Physics*, *10*(7), 3365–3383. doi: 10.5194/acp-10-3365-2010

Schmale, J., Henning, S., Decesari, S., Henzing, B., Keskinen, H., Sellegri, K., Ovadnevaite, J., Pöhlker, M. L., Brito, J., Bougiatioti, A., Kristensson, A., Kalivitis, N., Stavroulas, I., Carbone, S., Jefferson, A., Park, M., Schlag, P., Iwamoto, Y., Aalto, P., Äijälä, M., Bukowiecki, N., Ehn, M., Frank, G., Fröhlich, R., Frumau, A., Herrmann, E., Herrmann, H., Holzinger, R., Kos, G., Kulmala, M., Mihalopoulos, N., Nenes, A., O'Dowd, C., Petäjä, T., Picard, D., Pöhlker, C., Pöschl, U., Poulain, L., Prévôt, A. S. H., Swietlicki, E., Andreae, M. O., Artaxo, P., Wiedensohler, A., Ogren, J., Matsuki, A., S, Y. S., Stratmann, F., Baltensperger, U., & Gysel, M. (2018). Long-term cloud condensation nuclei number concentration, particle number size distribution and chemical composition measurements at regionally representative observatories. *Atmospheric Chemistry and Physics*, *18*(4), 2853–2881. doi: 10.5194/acp-18-2853-2018

Singh, V. P. (2016). Incidence of Temperature Inversion and their Impact on Air Quality: A Case Study of Delhi. In *AGU Fall Meeting Abstracts* (Vol. 2016, pp. A51D–0082). Retrieved from `https://ui.adsabs.harvard.edu/abs/2016AGUFM.A51D0082S`

Stein, A. F., Draxler, R. R., Rolph, G. D., Stunder, B. J. B., Cohen, M. D., & Ngan, F. (2015). NOAA's HYSPLIT atmospheric transport and dispersion modelling system. *Bulletin of the American Meteorological Society*, *96*(12), 2059–2077. doi: 10.1175/BAMS-D-14-00110.1

Still, M., Venzke, H., Durst, F., & Melling, A. (1998). Influence of humidity on the convective heat transfer from small cylinders. *Experiments in Fluids*, *24*(2), 141–150. doi: 10.1007/s003480050161

Stocker, T., Qin, D., Plattner, G.-K., Tignor, M., Allen, S., Boschung, J., Nauels, A., Xia, Y., Bex, V., Midgley, P., & (eds.). (2013). IPCC, 2013: Climate Change 2013: The Physical Science Basis. Contribution of Working Group I to the Fifth Assessment Report of the Intergovernmental Panel on Climate Change. *Cambridge University Press, Cambridge, United Kingdom and New York, NY, USA*.

Stull, R. B. (2012). *An introduction to boundary layer meteorology* (Vol. 13). Springer Science & Business Media.

Su, H., Cheng, Y., & Pöschl, U. (2020). New Multiphase Chemical Processes Influencing Atmospheric Aerosols, Air Quality, and Climate in the Anthropocene. *Accounts of Chemical Research*, *53*(10), 2034–2043. doi: 10.1021/acs.accounts.0c00246

Su, T., Li, Z., Zheng, Y., Luan, Q., & Guo, J. (2020). Abnormally shallow boundary layer associated with severe air pollution during the COVID-19 lockdown

in China. *Geophysical Research Letters*, *47*(20), e2020GL090041. doi: 10.1029/2020GL090041

Thomas, A., Sarangi, C., & Kanawade, V. P. (2019). Recent increase in winter hazy days over Central India and the Arabian Sea. *Scientific Reports*, *9*(1), 1–10. doi: 10.1038/s41598-019-53630-3

Tie, X., Huang, R.-J., Cao, J., Zhang, Q., Cheng, Y., Su, H., Chang, D., Pöschl, U., Hoffmann, T., Dusek, U., Li, G., Worsnop, D. R., & O'Dowd, C. D. (2017). Severe pollution in China amplified by atmospheric moisture. *Scientific Reports*, *7*(1), 1–8. doi: 10.1038/s41598-017-15909-1

Tiwari, S., Srivastava, A. K., Bisht, D. S., Parmita, P., Srivastava, M. K., & Attri, S. (2013). Diurnal and seasonal variations of black carbon and PM2. 5 over New Delhi, India: Influence of meteorology. *Atmospheric Research*, *125*, 50–62. doi: 10.1016/j.atmosres.2013.01.011

Twomey, S. (1959). The nuclei of natural cloud formation part II: The supersaturation in natural clouds and the variation of cloud droplet concentration. *Geofisica pura e applicata*, *43*(1), 243–249. doi: 10.1007/BF01993560

Van Rossum, G., & Drake, F. L. (2009). *Python 3 Reference Manual*. Scotts Valley, CA: CreateSpace.

Waggoner, A. P., Weiss, R. E., Ahlquist, N. C., Covert, D. S., Will, S., & Charlson, R. J. (1981). Optical characteristics of atmospheric aerosols. *Atmospheric Environment (1967)*, *15*(10), 1891–1909. doi: 10.1016/0004-6981(81)90224-9

Wang, J., Wang, S., Jiang, J., Ding, A., Zheng, M., Zhao, B., Wong, D. C., Zhou, W., Zheng, G., Wang, L., Pleim, J. E., & Hao, J. (2014). Impact of aerosol–meteorology interactions on fine particle pollution during China's severe haze episode in January 2013. *Environmental Research Letters*, *9*(9), 094002. doi: 10.1088/1748-9326/9/9/094002

Wang, Y., & Chen, Y. (2019). Significant climate impact of highly hygroscopic atmospheric aerosols in Delhi, India. *Geophysical Research Letters*, *46*(10), 5535–5545. doi: 10.1029/2019GL082339

Wang, Y., Niu, S., Lv, J., Lu, C., Xu, X., Wang, Y., Ding, J., Zhang, H., Wang, T., & Kang, B. (2019). A new method for distinguishing unactivated particles in cloud condensation nuclei measurements: Implications for aerosol indirect effect evaluation. *Geophysical Research Letters*, *46*(23), 14185–14194. doi: 10.1029/2019GL085379

Wang, Y., Yu, M., Wang, Y., Tang, G., Song, T., Zhou, P., Liu, Z., Hu, B., Ji, D., Wang, L., Zhu, X., Yan, C., Ehn, M., Gao, W., Pan, Y., Xin, J., Sun, Y., Kerminen, V.-M., Kulmala, M., & Petäjä, T. (2020). Rapid formation of intense haze episodes via aerosol–boundary layer feedback in Beijing. *Atmospheric Chemistry and Physics*, *20*(1), 45–53. doi: 10.5194/acp-20-45-2020

Wiedensohler, A. (1988). An approximation of the bipolar charge distribution for particles in the submicron size range. *Journal of Aerosol Science*, *19*(3), 387–389. doi: 10.1016/0021-8502(88)90278-9

Wu, J., Bei, N., Hu, B., Liu, S., Zhou, M., Wang, Q., Li, X., Liu, L., Feng, T., Liu, Z., Wang, Y., Cao, J., Tie, X., Wang, J., Molina, L. T., & Li, G. (2019). Aerosol–radiation feedback deteriorates the wintertime haze in the North China Plain. *Atmospheric Chemistry and Physics*, *19*(13), 8703–8719. doi: 10.5194/acp-19-8703-2019

Wu, Z., Chen, J., Wang, Y., Zhu, Y., Liu, Y., Yao, B., Zhang, Y., & Hu, M. (2018). Interactions between water vapor and atmospheric aerosols have key roles in air quality and climate change. *National Science Review*, *5*(4), 452–454. doi: 10.1093/nsr/nwy063

Yu, J., Wang, Y., & Liu, M. (2020). Mechanisms of an extreme fog and haze event in the megacities of central and eastern China. *Meteorology and Atmospheric*

Physics, 1–17. doi: 10.1007/s00703-020-00737-2

Zheng, G. J., Duan, F. K., Su, H., Ma, Y. L., Cheng, Y., Zheng, B., Zhang, Q., Huang, T., Kimoto, T., Chang, D., Pöschl, U., Cheng, Y. F., & He, K. B. (2015). Exploring the severe winter haze in Beijing: the impact of synoptic weather, regional transport and heterogeneous reactions. *Atmospheric Chemistry and Physics*, *15*(6), 2969–2983. doi: 10.5194/acp-15-2969-2015

Supporting Information for "Planetary boundary layer height modulates aerosol – water vapour interactions during winter in the megacity of Delhi"

Subha S. Raj[1,2], Ovid O. Krüger[3], Amit Sharma[1,a], Upasana Panda[1,4], Christopher Pöhlker[3], David Walter[3], Jan-David Förster[3], Rishi Pal Singh[5], Swetha S.[1,b], Thomas Klimach[3], Eoghan Darbyshire[6,c], Scot T. Martin[7,8], Gordon McFiggans[6], Hugh Coe[6], James Allan[6,9], Ravikrishna R.[10,2], Vijay Kumar Soni[5], Hang Su[3], Meinrat O. Andreae[3,11,12], Ulrich Pöschl[3], Mira L. Pöhlker[3]and Sachin S. Gunthe[1,2]

[1]EWRE Division, Department of Civil Engineering, Indian Institute of Technology Madras, Chennai, India

[2]Laboratory for Atmospheric and Climate Sciences, Indian Institute of Technology Madras, Chennai, India

[3]Multiphase Chemistry and Biogeochemistry Departments, Max Planck Institute for Chemistry, Mainz, Germany

[4]Department of Environment and Sustainability, CSIR Institute of Minerals and Materials Technology, Bhubaneswar, India

[5]India Meteorological Department, New Delhi, India

[6]Department of Earth and Environmental Sciences, School of Natural Sciences, University of Manchester, Manchester, UK

[7]John A. Paulson School of Engineering and Applied Sciences, Harvard University, Cambridge, MA, USA

[8]Department of Earth and Planetary Sciences, Harvard University, Cambridge, MA, USA

[9]National Centre for Atmospheric Science, University of Manchester, Manchester, UK

[10]Department of Chemical Engineering, Indian Institute of Technology Madras, Chennai, India

[11]Scripps Institution of Oceanography, University of California San Diego, La Jolla, CA, USA

[12]Department of Geology and Geophysics, King Saud University, Riyadh, Saudi Arabia

[a]now at: Department of Civil and Infrastructure Engineering, Indian Institute of Technology Jodhpur, Karwar, Jodhpur, India

[b]now at: CSIR Fourth Paradigm Institute, Bengaluru, India

August 9, 2021, 8:56am

[c]now at: The Conflict and Environment Observatory, Hebden Bridge, West Yorkshire, UK

Corresponding author: Subha S. Raj (subhasraj89@gmail.com), Mira L. Pöhlker(m.pohlker@mpic.de), Sachin S. Gunthe (s.gunthe@iitm.ac.in)

Contents of this file

1. Text S1 to S2
2. Figures S1 to S12
3. Tables S1 to S5

Additional Supporting Information (Files uploaded separately)

1. Caption for Dataset S1

Introduction

The data set provided in .csv format contains the PBL height using various model simulations used in this study.

Supporting explanations, measurement data, and analysis results discussed in the manuscript are provided in the following figures and tables.

Text S1. We observed multiple periods with low solar radiation as shown in panel (b) of Figure S5. These periods could have faster nocturnal radiative cooling of the atmosphere and result in an increase in the inversion layer depth (Stull, 2012). These were classified as the weak inversion periods. During rest of the campaign, the strong solar radiation would have slowed down the nocturnal cooling of the atmosphere. Also the high RH near surface observed during these periods could have caused more heat transfer to the atmosphere above the ground (Pasricha et al., 2003; Still et al., 1998). This results in the surface air being cooler than the air above it and cause lowering of the planetary boundary layer height (H_{BL}). These periods were classified as the strong inversion periods. The above observation and hypothesis fits well with the PBL simulations by WRF model, which showed higher H_{BL} during nighttime of weak inversion periods and lower H_{BL} during nighttime of strong inversion periods. The daytime H_{BL} remained high for both the periods.

Text S2 The 3-day air mass back trajectories (BT) in the top panel of Figure S6 and the bottom panel of Figure S7 shows longer trajectories compared to that showed in the bottom panel of Figure S9, because a constant height of 1000 m was selected in the former as the top of the HYSPLIT model (Stein et al., 2015). The same analysis was done using the WRF modelled H_{BL} as the top of the model, which resulted in similar but shorter BTs as shown in Figure S9.

Data Set S1. Time series data of model simulations of planetary boundary layer height (H_{BL}; m) using the WRF and the HYSPLIT model from 05 Feb to 02 Mar 2018. The first column contains the date and time in Indian Standard time (UTC + 05:30) of each entry of H_{BL} simulations in the remaining columns. The second and third column contains the

simulations of WRF using the Bulk-Richardson number method and the TKE method respectively. The fourth column contains the mixing depth values from HYSPLIT model.

References

Pasricha, P. K., Gera, B. S., Shastri, S., Maini, H. K., John, T., Ghosh, A. B., ... Garg, S. C. (2003). Role of the water vapour greenhouse effect in the forecasting of fog occurrence. *Boundary-Layer Meteorology*, *107*(2), 469–482. doi: 10.1023/A:1022128800130

Stein, A. F., Draxler, R. R., Rolph, G. D., Stunder, B. J. B., Cohen, M. D., & Ngan, F. (2015). NOAA's HYSPLIT atmospheric transport and dispersion modelling system. *Bulletin of the American Meteorological Society*, *96*(12), 2059–2077. doi: 10.1175/BAMS-D-14-00110.1

Still, M., Venzke, H., Durst, F., & Melling, A. (1998). Influence of humidity on the convective heat transfer from small cylinders. *Experiments in Fluids*, *24*(2), 141–150. doi: 10.1007/s003480050161

Stull, R. B. (2012). *An introduction to boundary layer meteorology* (Vol. 13). Springer Science & Business Media.

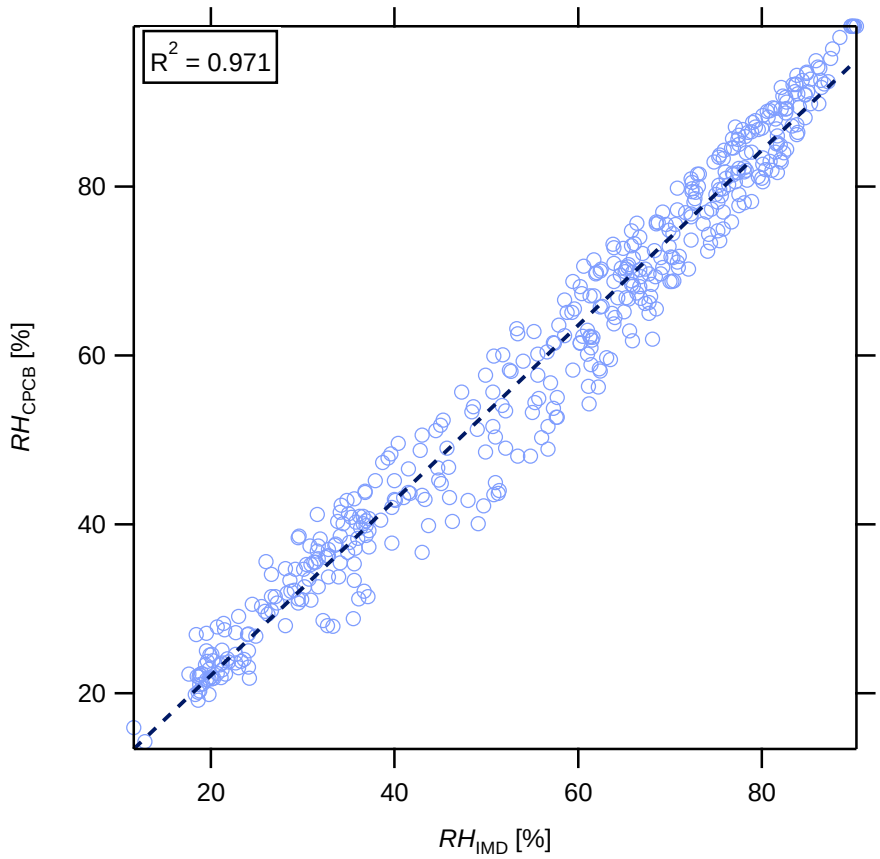

Figure S1. Correlation between concomitant relative humidity measurements in India Meteorological Department (IMD) or the campaign site and the Central Pollution Control Board site (CPCB).

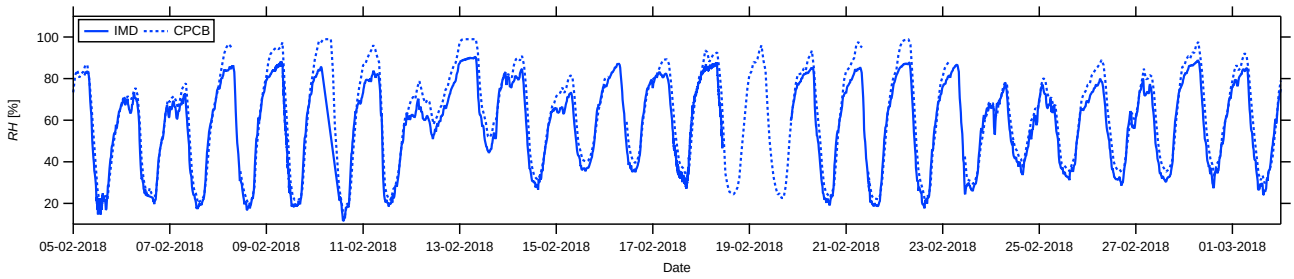

Figure S2. Temporal evolution of concomitant relative humidity measurements in India Meteorological Department (IMD) or the campaign site and the Central Pollution Control Board site (CPCB).

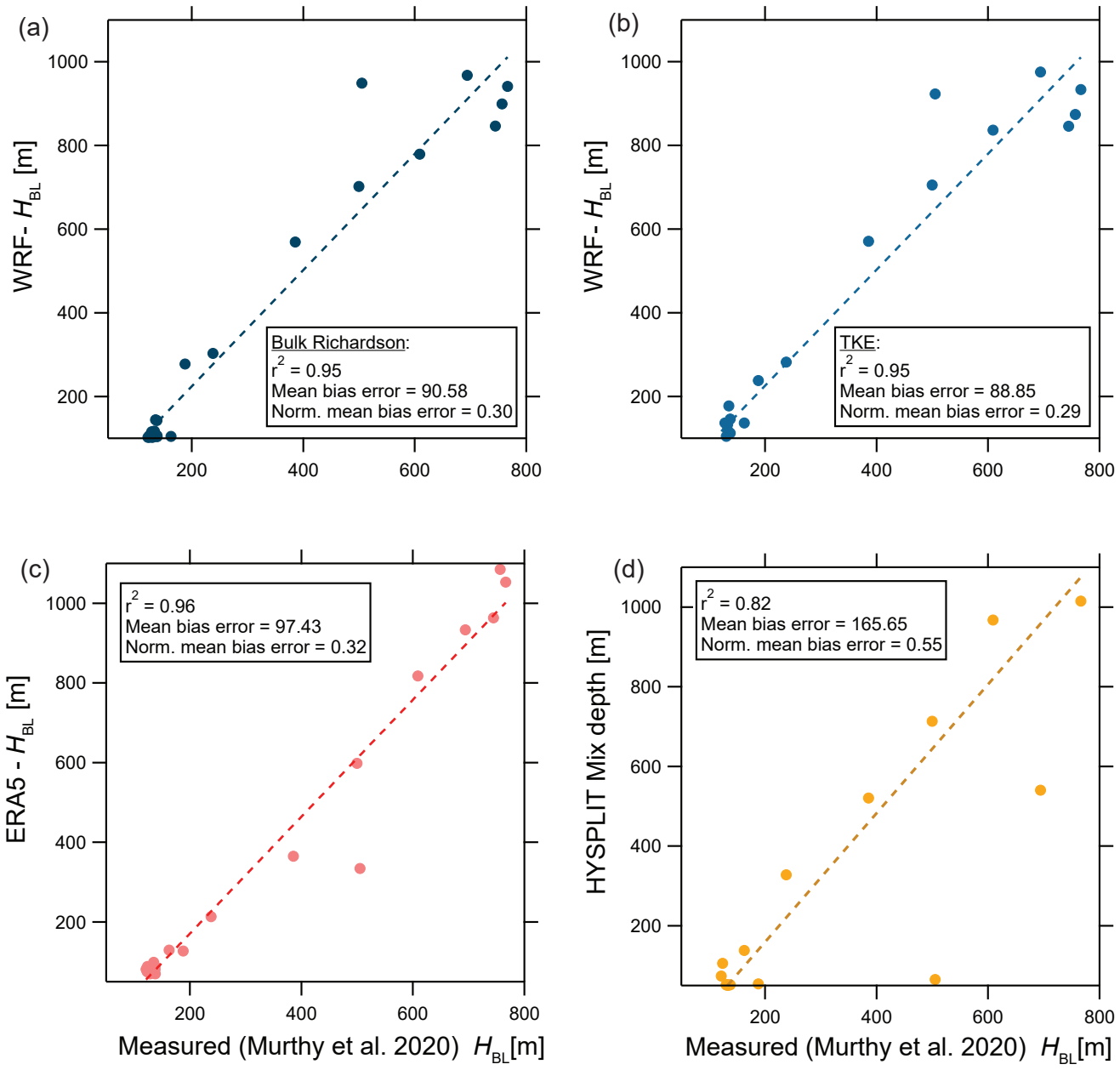

Figure S3. Comparison of modelled planetary boundary layer height from (a): WRF model using Bulk Richardson number, (b) in WRF model using turbulence kinetic energy (TKE), (c) ECMWF satellite reanalysis data (ERA5) and (d) HYSPLIT model with measured data is shown as correlation plots.

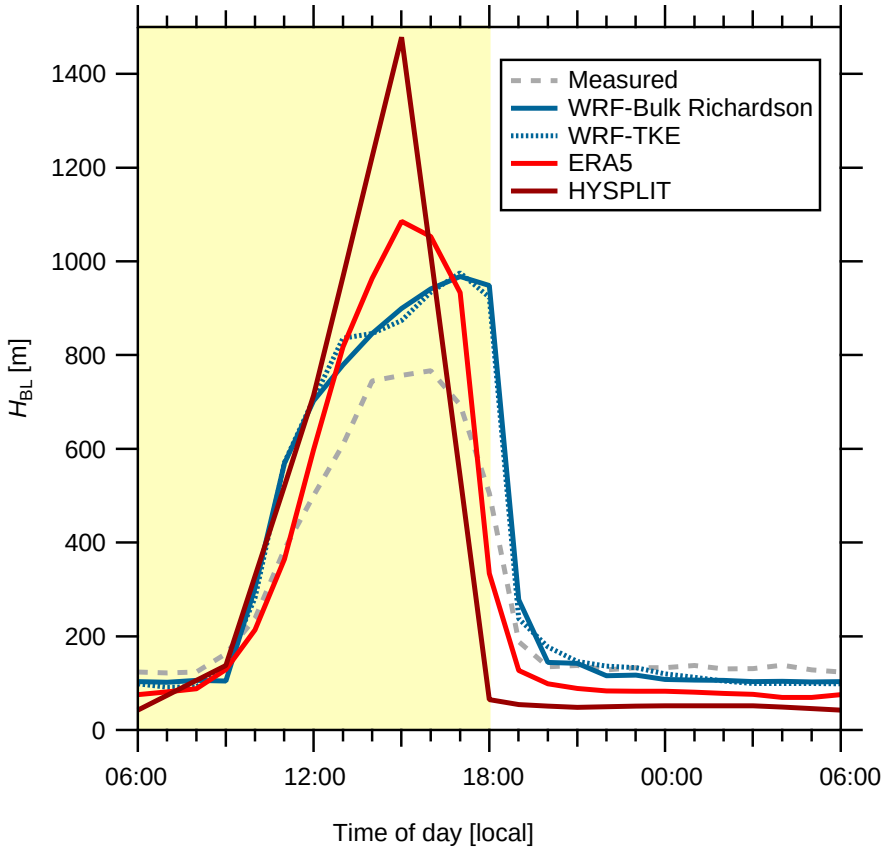

Figure S4. The campaign-average diurnal variation of planetary boundary layer height (H_{BL}): modeled by the WRF model using Bulk Richardson number method (blue solid line) and TKE method (blue dotted line); ECMWF satellite reanalysis ERA5 data (light red solid line); HYSPLIT model (dark red solid line); measured by ceilometer (grey dashed line).

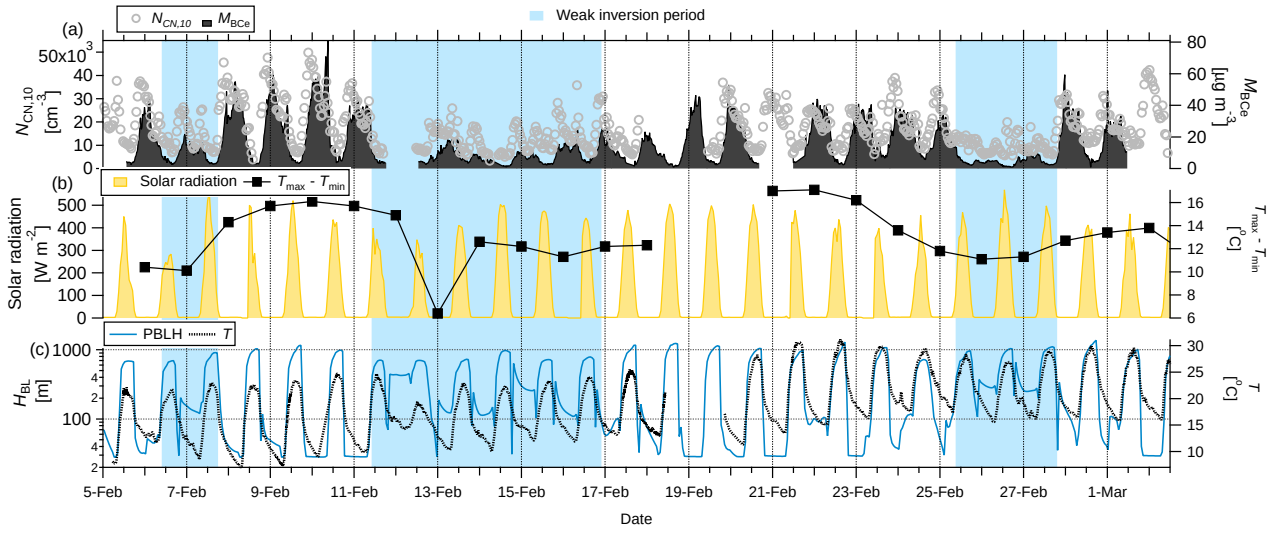

Figure S5. Temporal evolution of the (a): Total particle number concentration in the size range ∼10 to 370 nm ($N_{\mathrm{CN},10}$, cm^{-3}) on the left axis and mass concentration of equivalent BC ($M_{\mathrm{BC,e}}$, μg m^{-3}) on the right axis; (b): Solar radiation (W m^{-2}) on the left axis and difference between maximum and minimum temperature in the period, 12:00:00 LT to 11:59:59 LT (T_{max} - T_{min}, °C) of each diurnal cycle; (c): Planetary boundary layer height (H_{BL}) modelled in WRF using Bulk Richardson number method on the left axis and temperature (T, °C)on the right axis.

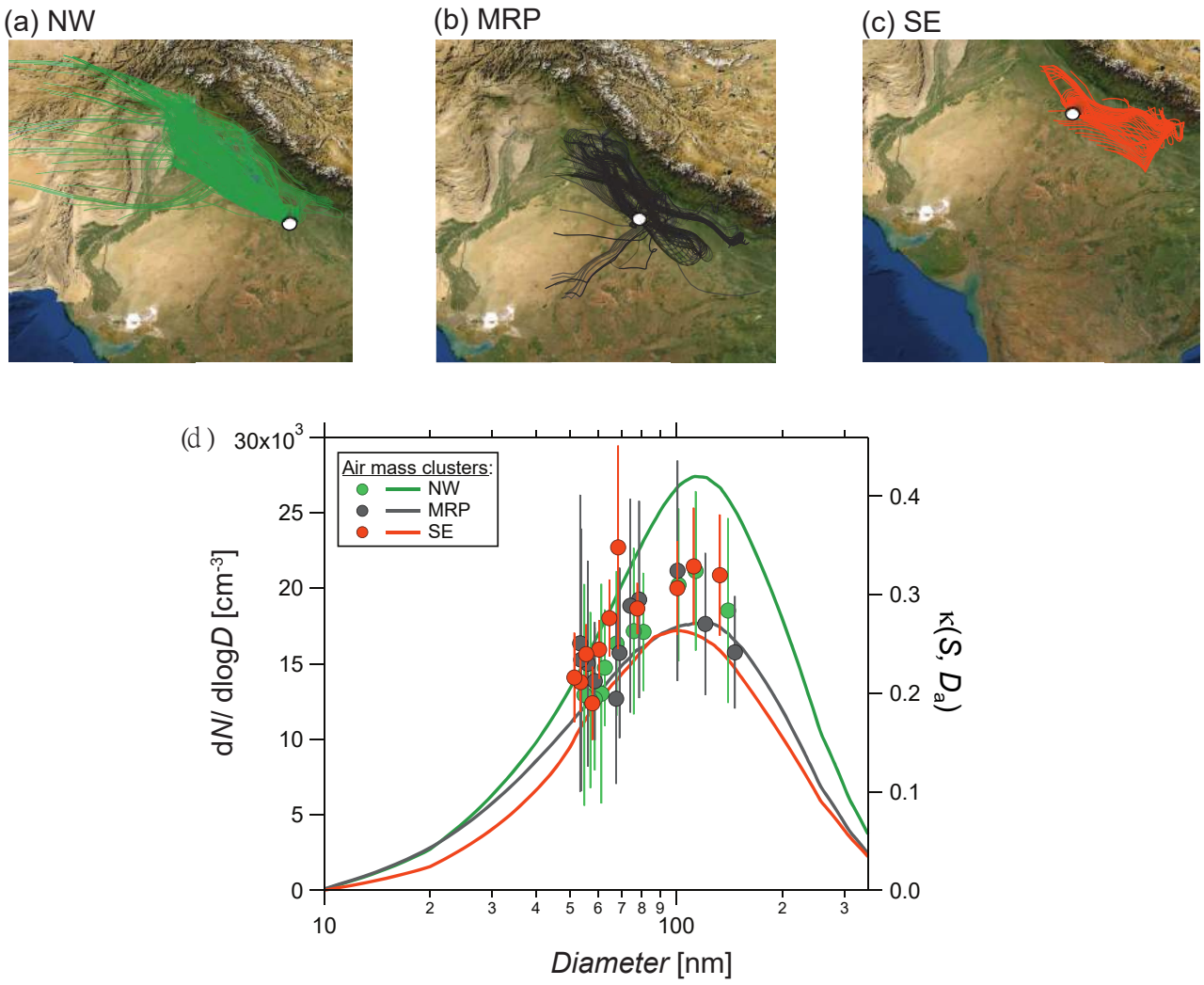

Figure S6. The 3-day back trajectory during (a): NW air mass, (b): MRP air mass and (c): SE air mass is shown. The white dot denotes the location of campaign site in Delhi. The average aerosol number size distribution (left axis) and hygroscopicity distribution (right axis) during each air mass is shown in (c).

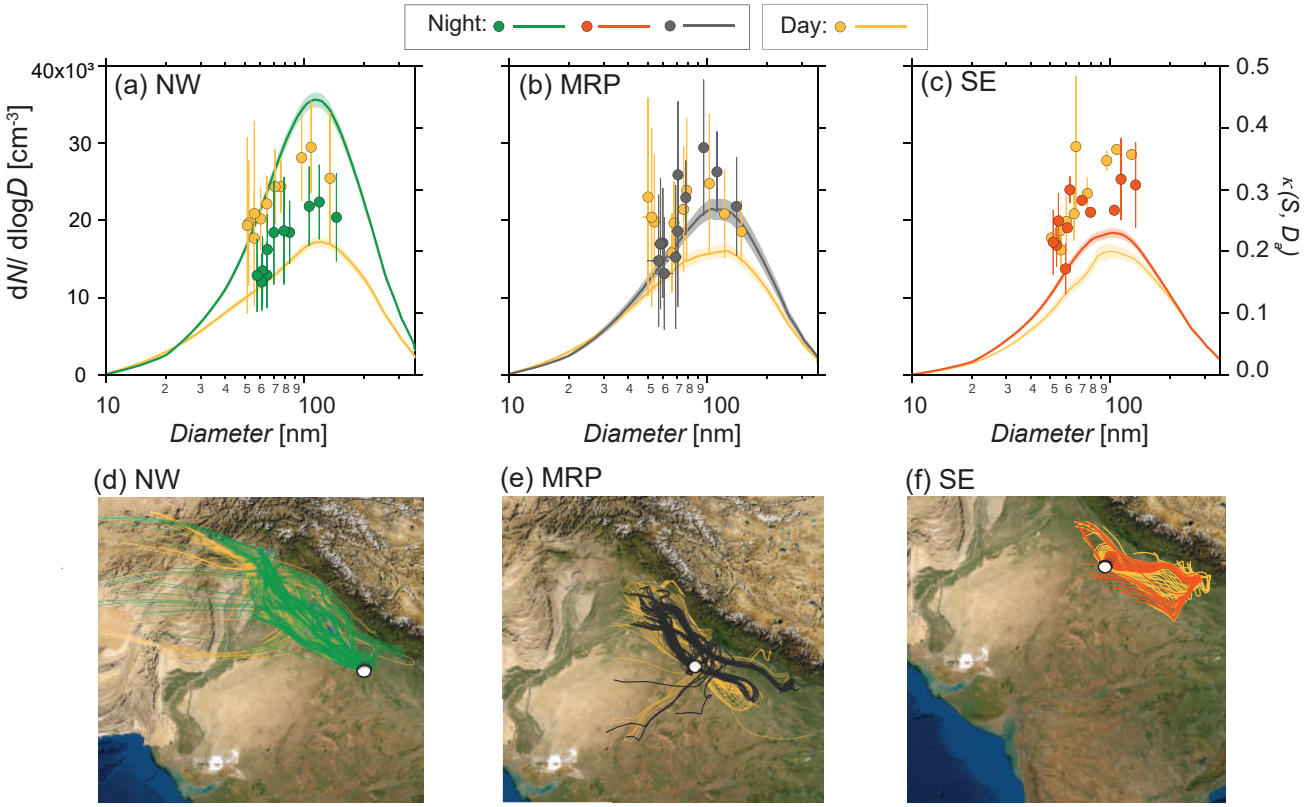

Figure S7. The average aerosol number size distribution (left axis) and hygroscopicity distribution (right axis) during (a): NW air mass, (b): MRP air mass and (c): SE air mass resolved into daytime (yellow) and nighttime (colour of respective air mass) are shown.The 3-day back trajectory resolved into daytime (yellow) and nighttime (colour of respective air mass) during (a): NW air mass, (b): MRP air mass and (c): SE air mass is shown. The white dot denotes the location of campaign site in Delhi.

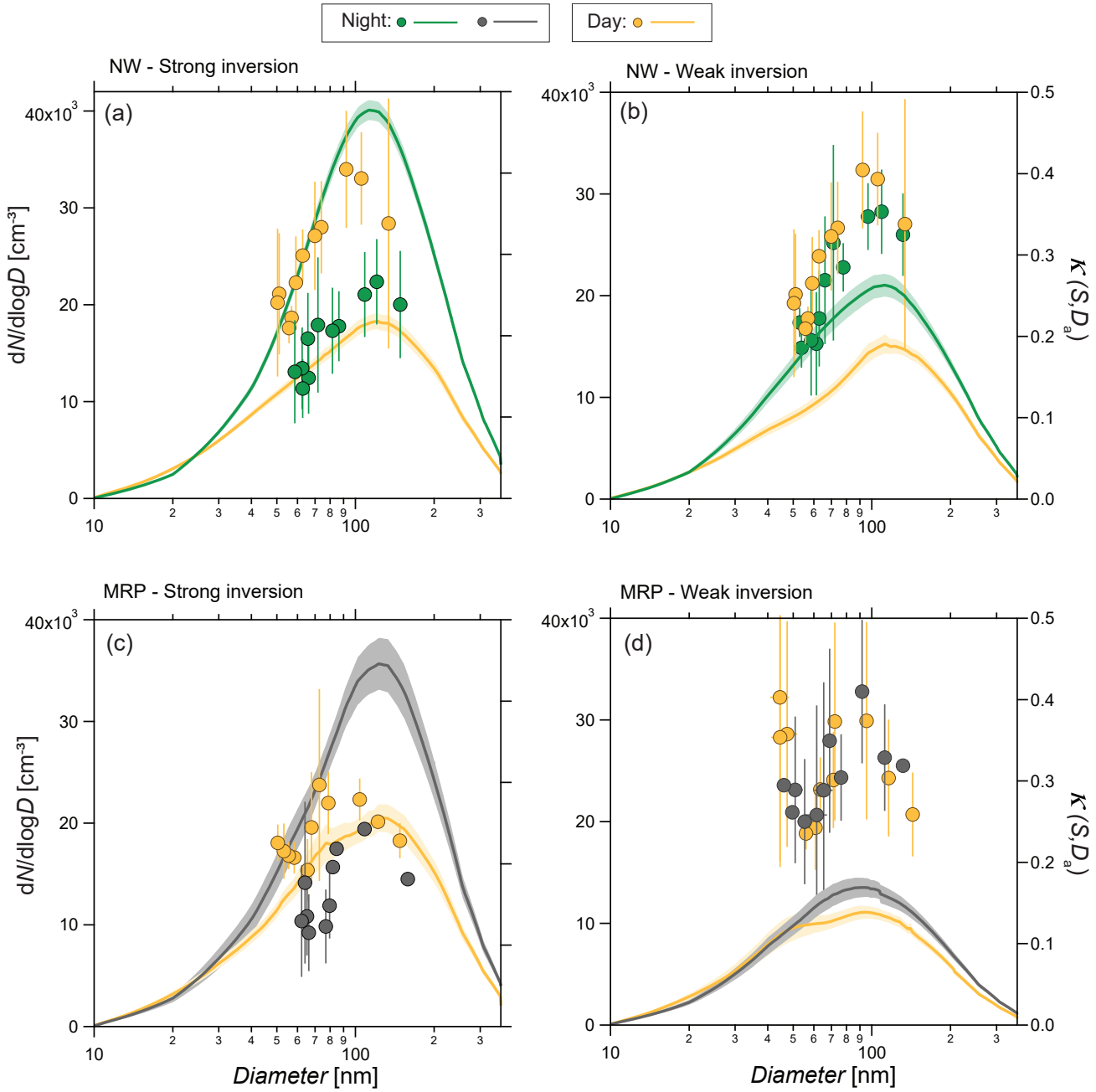

Figure S8. Average aerosol number size distribution (left axis) and hygroscopicity distribution (right axis) during daytime and nighttime for (a): NW under strong inversion periods; (b): NW under weak inversion periods; (c): MRP under strong inversion periods and (d): MRP under weak inversion periods.

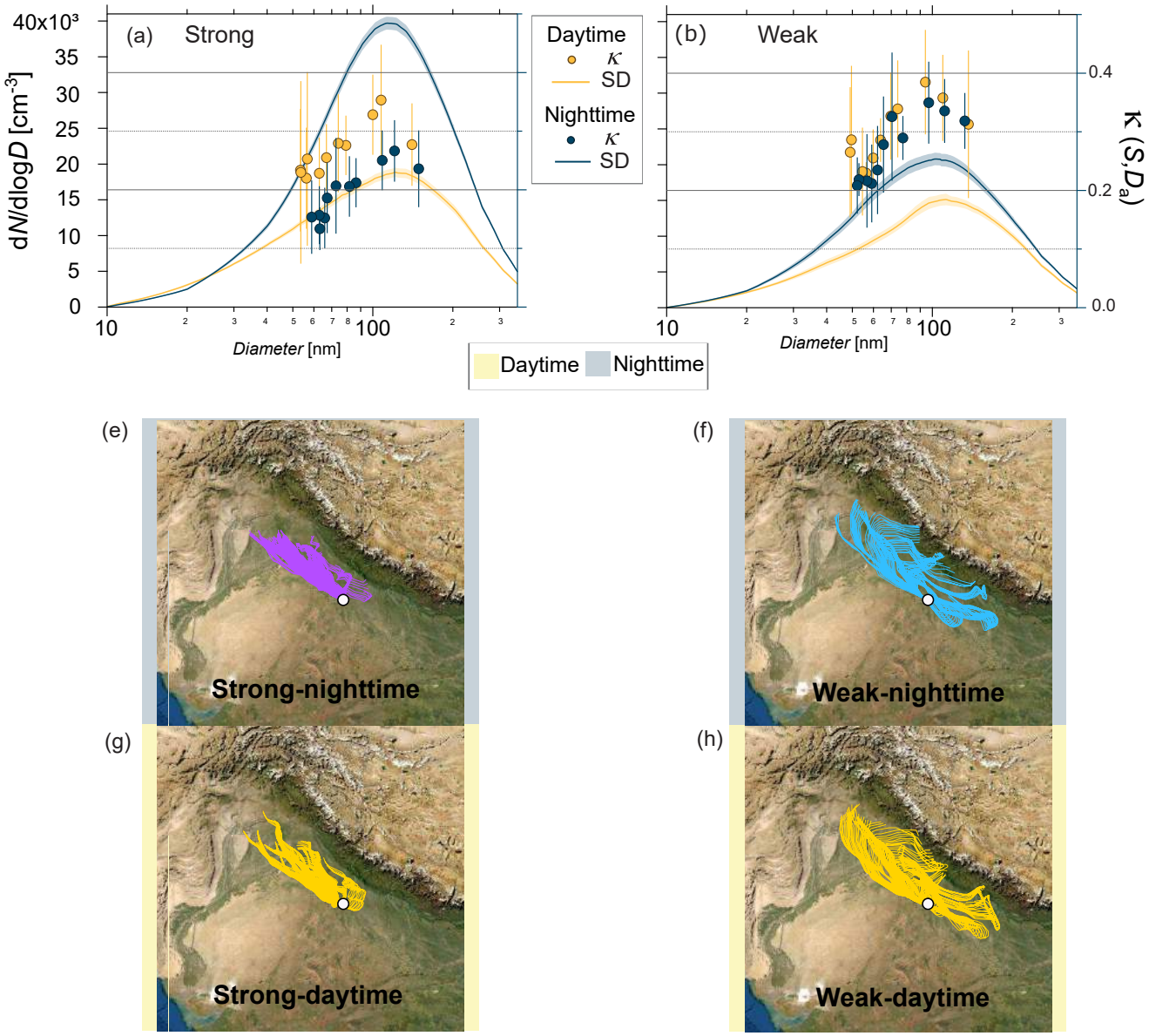

Figure S9. Average aerosol number size distribution (left axis) and hygroscopicity distribution (right axis) during daytime and nighttime for (a): Strong inversion periods and (b): Weak inversion periods. The 3-day back trajectories retrieved using the WRF modelled H_{BL} as the top of model are shown during, (e) strong inversion-nighttime (f) weak inversion-nighttime, (g) strong inversion-daytime and (h) weak inversion-daytime. The white dot denotes the location of campaign site in Delhi.

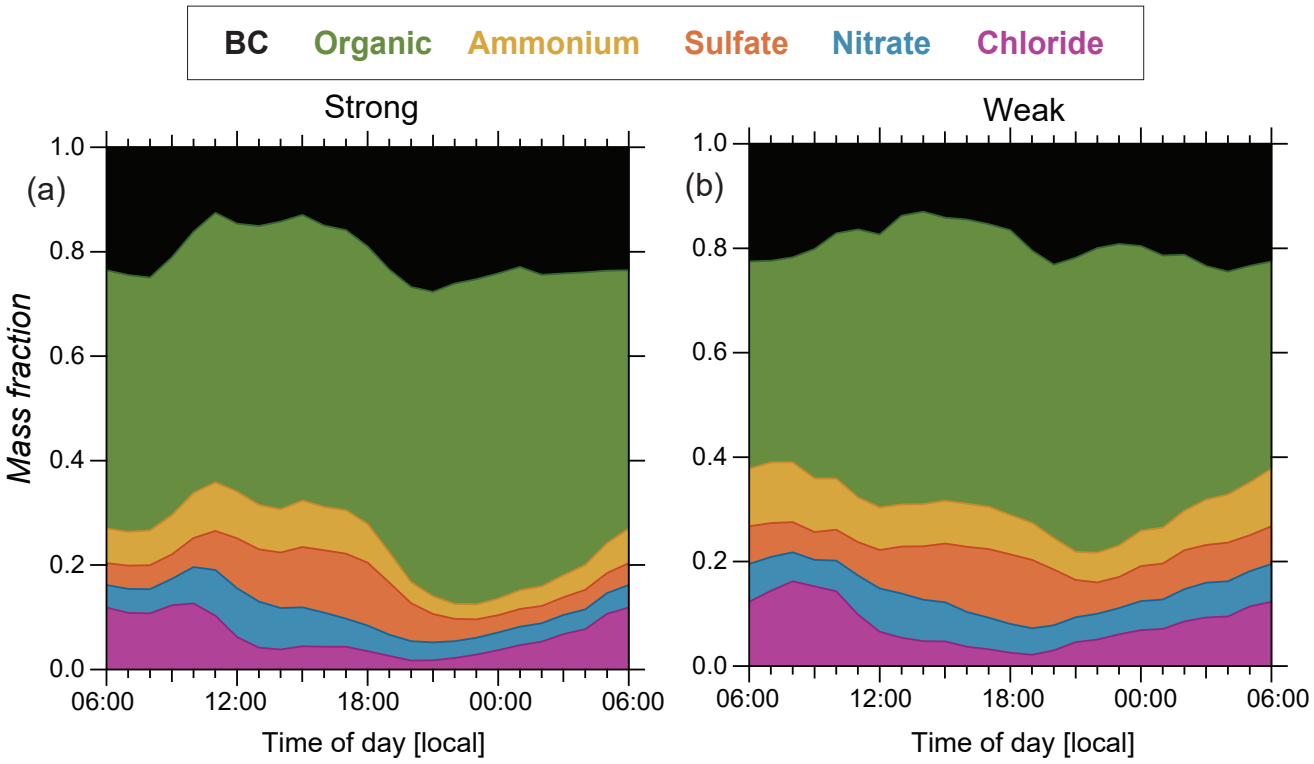

Figure S10. Average diurnal variation of NR-PM1 components such as BC, organics, ammonium, sulfate, nitrate and chloride during (a): strong inversion periods and (b): weak inversion periods.

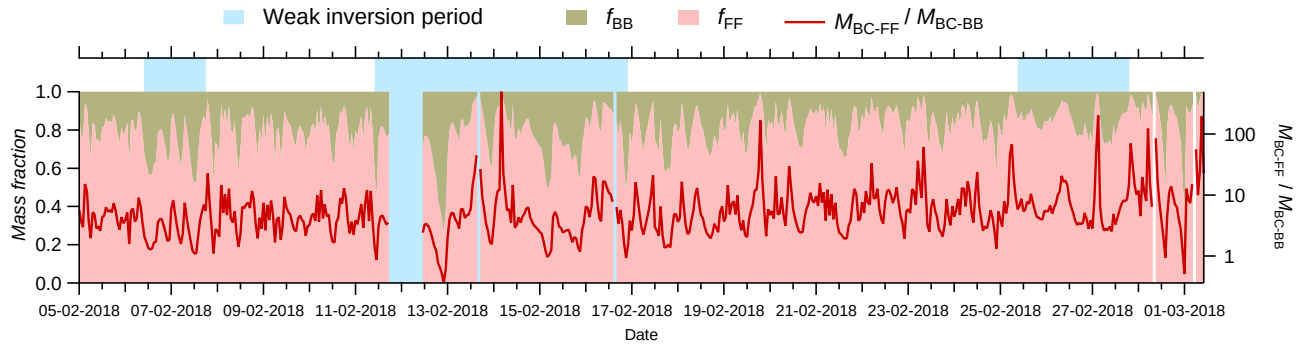

Figure S11. Temporal evolution of the mass fractions of equivalent black carbon (BC) associated with biomass burning (f_{BB}) and fossil fuel combustion (f_{FF}) on the left axis; ratio of mass of equivalent BC associated with fossil fuel combustion to that associated with biomass burning ($M_{\mathrm{BC\text{-}FF}}$ / $M_{\mathrm{BC\text{-}BB}}$)

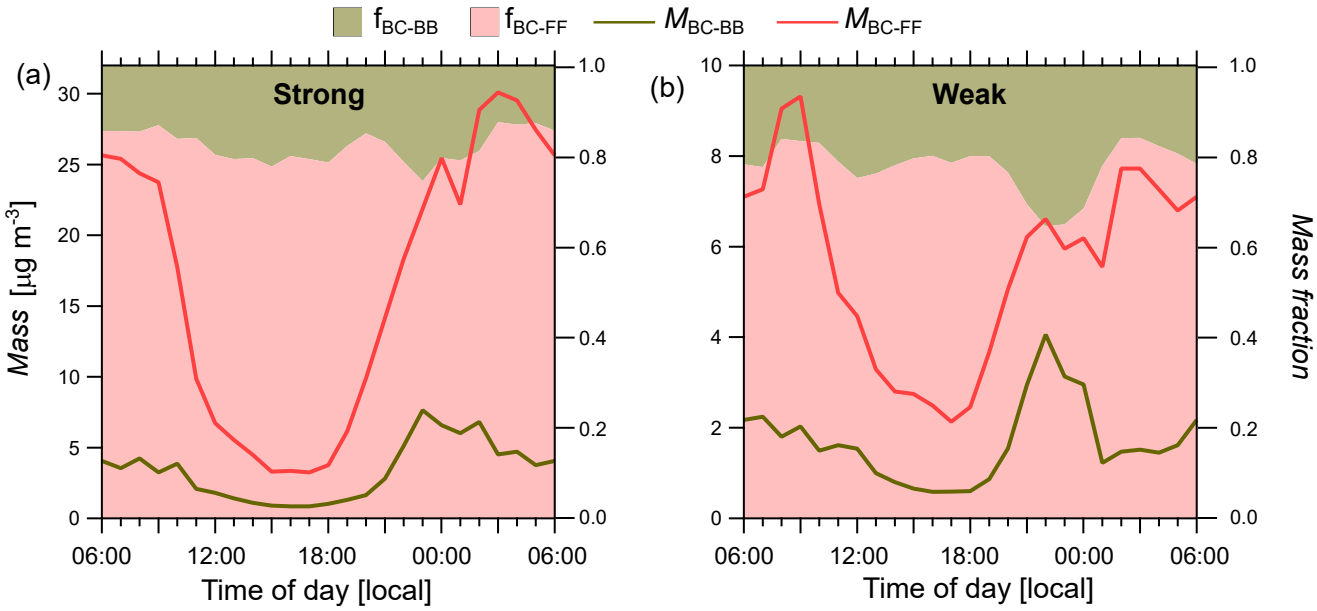

Figure S12. Average diurnal variation of mass of equivalent black carbon associated with biomass burning ($M_{\mathrm{BC\text{-}BB}}$) and fossil fuel combustion ($M_{\mathrm{BC\text{-}FF}}$) on the left axis; and fraction of equivalent black carbon associated with biomass burning ($f_{\mathrm{BC\text{-}BB}}$) and fossil fuel combustion ($f_{\mathrm{BC\text{-}FF}}$) on the right axis for (a): strong inversion and (b): weak inversion periods.

Table S1. Comparison of modelled planetary boundary layer height using different methods with measured data is tabulated.

	WRF-Bulk Richardson	WRF-TKE	ERA5	HYSPLIT
Mean bias error	90.58	88.85	97.43	165.65
Normalized mean bias error	0.30	0.29	0.32	0.55

Table S2. The time of occurrence of strong and weak inversion periods during the campaign is tabulated. All dates indicate year 2018 and all times are in local time (UTC + 05:30).

Period	Time of occurrence
Strong inversion	05 Feb 00:30 to 06 Feb 09:30
	07 Feb 19:30 to 11 Feb 09:30
	16 Feb 22:30 to 25 Feb 08:30
	27 Feb 20:30 to 02 Mar 23:30
Weak inversion	06 Feb 10:30 to 07 Feb 18:30
	11 Feb 10:30 to 16 Feb 21:30
	25 Feb 09:30 to 27 Feb 19:30

Table S3. Probability (%) of occurrence of strong inversion nighttime, weak inversion nighttime and daytime in each H_{BL} bin. H_{BL} bins are defines as minimum to 1st quartile, 1st to 2nd quartile, 2nd to 3rd quartile and 3rd quartile to maximum.

H_{BL}:	28 to 50 m	50 to 158 m	158 to 685 m	685 to 1374 m
Strong-nighttime	60 %	34 %	5 %	1 %
Weak-nighttime	5 %	39 %	56 %	0 %
Daytime	9 %	13 %	28 %	49 %

Table S4. CCN properties measured during strong inversion periods resolved into daytime and nighttime in Delhi shown as a function of effective supersaturation achieved inside the CCNC. The S levels are average values measure with a standard deviation of ∼0.001 %. All other values are expressed as average ± standard deviation. Parameters tabulated are: midpoint activation diameter ($D_{\mathrm{a}}(S)$), hygroscopicity from size-resolved CCN measurements ($\kappa(S,\ D_a)$), width of the CCN activation curve ($\sigma(S)$), maximum activated fraction ($MAF(S)$), total CCN concentration ($N_{\mathrm{CCN}}(S)$), total particle concentration in the size range ∼10 to 370 nm ($N_{\mathrm{CN,10}}$), CCN efficiency ($N_{\mathrm{CCN}}(S)/N_{\mathrm{CN,10}}$), and number of samples for each S levels (n).

S [%]	$D_{\mathrm{a}}(S)$ [nm]	$\kappa(S,\ D_a)$	$\sigma(S)$ [nm]	$MAF(S)$	$N_{\mathrm{CCN}}(S)$ [cm^{-3}]	$N_{\mathrm{CN,10}}$ [cm^{-3}]	$N_{\mathrm{CCN}}(S)$ $/N_{\mathrm{CN,10}}$	n
Strong inversion-daytime:								
0.14	140 ± 12	0.28 ± 0.07	24 ± 7	0.91 ± 0.13	3527 ± 1793	13622 ± 5059	0.26 ± 0.10	18
0.17	110 ± 11	0.35 ± 0.09	20 ± 8	0.90 ± 0.14	4742 ± 2225	12799 ± 4240	0.36 ± 0.13	23
0.21	98 ± 9	0.33 ± 0.07	24 ± 10	0.96 ± 0.09	6845 ± 2995	14553 ± 5513	0.47 ± 0.13	22
0.32	79 ± 7	0.28 ± 0.05	21 ± 8	0.95 ± 0.08	7661 ± 3958	14194 ± 7328	0.54 ± 0.10	20
0.36	74 ± 8	0.28 ± 0.08	19 ± 10	0.94 ± 0.10	8760 ± 5323	15249 ± 7972	0.57 ± 0.12	19
0.43	67 ± 5	0.25 ± 0.06	20 ± 6	0.98 ± 0.08	10275 ± 5707	15256 ± 6921	0.66 ± 0.13	20
0.50	63 ± 7	0.23 ± 0.06	18 ± 6	0.95 ± 0.11	10813 ± 6696	15625 ± 7404	0.66 ± 0.13	20
0.58	57 ± 7	0.25 ± 0.15	15 ± 4	0.99 ± 0.08	12607 ± 8411	16570 ± 9996	0.74 ± 0.10	19
0.61	56 ± 6	0.22 ± 0.09	16 ± 6	0.98 ± 0.08	11553 ± 6744	15729 ± 7709	0.72 ± 0.13	21
0.65	53 ± 7	0.23 ± 0.10	15 ± 10	0.99 ± 0.06	12212 ± 6347	16123 ± 6836	0.74 ± 0.12	18
0.69	54 ± 10	0.23 ± 0.16	14 ± 7	0.99 ± 0.08	9647 ± 4036	13506 ± 4003	0.70 ± 0.12	19
Strong inversion-nighttime								
0.14	149 ± 15	0.24 ± 0.07	33 ± 9	0.69 ± 0.15	6155 ± 3062	28042 ± 7231	0.22 ± 0.11	22
0.17	121 ± 7	0.27 ± 0.05	30 ± 5	0.72 ± 0.15	8570 ± 3986	26092 ± 7074	0.33 ± 0.14	22
0.21	109 ± 8	0.25 ± 0.05	33 ± 6	0.75 ± 0.15	10271 ± 4609	26265 ± 7610	0.39 ± 0.14	21
0.32	86 ± 6	0.21 ± 0.04	28 ± 5	0.79 ± 0.13	13748 ± 5542	26171 ± 8206	0.53 ± 0.15	21
0.36	82 ± 7	0.21 ± 0.05	27 ± 8	0.82 ± 0.12	14934 ± 5893	26233 ± 8750	0.57 ± 0.13	22
0.43	73 ± 8	0.21 ± 0.08	25 ± 7	0.79 ± 0.13	14542 ± 7099	25605 ± 9825	0.57 ± 0.14	20
0.50	67 ± 7	0.19 ± 0.06	22 ± 12	0.81 ± 0.13	15615 ± 7545	25338 ± 9344	0.61 ± 0.14	21
0.58	66 ± 7	0.15 ± 0.05	24 ± 9	0.80 ± 0.12	15404 ± 8335	24635 ± 9083	0.60 ± 0.15	23
0.61	63 ± 9	0.16 ± 0.05	23 ± 10	0.82 ± 0.12	17373 ± 7533	27042 ± 7815	0.63 ± 0.16	22
0.65	63 ± 7	0.13 ± 0.04	22 ± 7	0.82 ± 0.12	17049 ± 6846	26964 ± 7762	0.63 ± 0.15	24
0.69	59 ± 7	0.15 ± 0.06	20 ± 8	0.87 ± 0.12	18289 ± 7678	26237 ± 8178	0.69 ± 0.15	25

Table S5. CCN properties measured during weak inversion periods resolved into daytime and nighttime in Delhi shown as a function of effective supersaturation achieved inside the CCNC. The S levels are average values measure with a standard deviation of ∼0.001 %. All other values are expressed as average ± standard deviation. Parameters tabulated are: midpoint activation diameter ($D_a(S)$), hygroscopicity from size-resolved CCN measurements ($\kappa(S,\ D_a)$), width of the CCN activation curve ($\sigma(S)$), maximum activated fraction ($MAF(S)$), total CCN concentration ($N_{CCN}(S)$), total particle concentration in the size range ∼10 to 370 nm ($N_{CN,10}$), CCN efficiency ($N_{CCN}(S)/N_{CN,10}$), and number of samples for each S levels (n).

S [%]	$D_a(S)$ [nm]	$\kappa(S,\ D_a)$	$\sigma(S)$ [nm]	$MAF(S)$	$N_{CCN}(S)$ [cm^{-3}]	$N_{CN,10}$ [cm^{-3}]	$N_{CCN}(S)$ /$N_{CN,10}$	n
Weak inversion-daytime:								
0.14	137 ± 14	0.31 ± 0.13	22 ± 6	0.98 ± 0.05	3079 ± 1972	10546 ± 4584	0.28 ± 0.09	15
0.17	109 ± 8	0.36 ± 0.07	18 ± 5	0.99 ± 0.06	4279 ± 2158	9722 ± 3058	0.42 ± 0.12	16
0.21	94 ± 7	0.38 ± 0.09	15 ± 5	0.98 ± 0.08	4614 ± 1793	9131 ± 2625	0.50 ± 0.11	15
0.32	74 ± 5	0.34 ± 0.08	14 ± 5	0.98 ± 0.07	6469 ± 2299	10298 ± 3678	0.63 ± 0.07	14
0.36	70 ± 5	0.33 ± 0.07	14 ± 8	0.99 ± 0.10	6981 ± 3475	10525 ± 5166	0.67 ± 0.07	14
0.43	64 ± 3	0.29 ± 0.04	18 ± 10	0.99 ± 0.06	7625 ± 4722	11077 ± 6304	0.68 ± 0.09	12
0.50	60 ± 3	0.26 ± 0.05	14 ± 5	1.00 ± 0.04	7608 ± 3459	10804 ± 5471	0.71 ± 0.08	12
0.58	56 ± 1	0.23 ± 0.02	12 ± 5	1.01 ± 0.05	6828 ± 2792	9294 ± 3345	0.73 ± 0.06	10
0.61	55 ± 4	0.23 ± 0.08	14 ± 7	1.00 ± 0.06	7485 ± 2180	10982 ± 2966	0.69 ± 0.11	12
0.65	50 ± 5	0.29 ± 0.13	13 ± 6	1.00 ± 0.05	8768 ± 3145	11842 ± 4332	0.74 ± 0.08	12
0.69	49 ± 5	0.27 ± 0.11	10 ± 5	0.99 ± 0.04	10990 ± 6261	14443 ± 7412	0.75 ± 0.07	13
Weak inversion-nighttime								
0.14	132 ± 7	0.32 ± 0.05	20 ± 7	0.88 ± 0.08	3676 ± 1346	13525 ± 5833	0.29 ± 0.09	10
0.17	111 ± 6	0.34 ± 0.05	20 ± 8	0.88 ± 0.07	4888 ± 1972	13482 ± 6577	0.38 ± 0.06	9
0.21	97 ± 6	0.35 ± 0.07	21 ± 8	0.88 ± 0.10	5286 ± 2567	12797 ± 5921	0.41 ± 0.11	11
0.32	77 ± 3	0.29 ± 0.04	22 ± 9	0.89 ± 0.10	6647 ± 2950	12589 ± 5010	0.53 ± 0.11	12
0.36	70 ± 7	0.33 ± 0.11	16 ± 6	0.86 ± 0.14	7461 ± 3072	13945 ± 5911	0.55 ± 0.13	13
0.43	65 ± 7	0.28 ± 0.08	19 ± 5	0.90 ± 0.09	8616 ± 3335	15079 ± 6813	0.61 ± 0.16	13
0.50	62 ± 6	0.23 ± 0.08	17 ± 5	0.90 ± 0.07	9896 ± 4043	16176 ± 7583	0.64 ± 0.11	11
0.58	59 ± 7	0.21 ± 0.07	15 ± 7	0.94 ± 0.05	10563 ± 4072	15656 ± 7043	0.70 ± 0.09	14
0.61	57 ± 8	0.22 ± 0.08	19 ± 16	0.95 ± 0.07	9951 ± 3245	14656 ± 6654	0.72 ± 0.11	11
0.65	53 ± 2	0.22 ± 0.03	13 ± 3	0.94 ± 0.06	9475 ± 4018	13231 ± 6221	0.73 ± 0.08	10
0.69	52 ± 4	0.21 ± 0.05	11 ± 3	0.95 ± 0.05	10411 ± 4267	13782 ± 5688	0.76 ± 0.07	10